UNIVERSITY OF GENOA

Ph.D. Program in
CLINICAL AND EXPERIMENTAL NEUROSCIENCE

MOLECULAR MECHANISMS AND THERAPEUTIC STRATEGIES IN CMT1 NEUROPATHIES

Tutor:
Prof. Marina Grandis
Dr. Lucilla Nobbio

Candidate:
Mattia Camera

XXXVIII CYCLE
2024/2025

Abstract

Charcot–Marie–Tooth (CMT) disease comprises a heterogeneous group of inherited peripheral neuropathies for which effective therapies are still lacking. Limited understanding of the molecular and developmental mechanisms underlying the most common CMT subtypes represents a major obstacle to therapeutic progress. This thesis addresses this gap by investigating two complementary aspects of CMT pathogenesis and treatment: the developmental origins of CMT1A neuropathy and a targeted therapeutic strategy for CMT1B.

In the first part of the work, we explored the early structural and molecular alterations occurring in a rat model of CMT1A. Through an integrated longitudinal approach combining high-resolution lipidomics and quantitative morphometric analyses, we characterized the maturation of peripheral myelin and myelinated fibers from early postnatal stages to adulthood. We demonstrate that CMT1A nerves exhibit a profound developmental delay, evident as early as postnatal day 20, affecting both myelin lipid composition and axonal growth. CMT1A myelin fails to become enriched in long-chain sphingolipids and retains features typical of unspecialized plasma membranes. These molecular abnormalities are paralleled by defective axonal enlargement, reduced fiber diameters, and persistent hypermyelination of small-caliber axons. Together, these findings indicate that CMT1A is primarily a disorder of impaired neurodevelopment and dysmyelination rather than progressive demyelination and identify a critical temporal window for potential therapeutic intervention.

In the second part, we focused on a CMT1B form caused by the dominant-negative heterozygous D61N mutation in the *MPZ* gene. Exploiting a knock-in mouse model faithfully recapitulating the human disease, we tested an allele-specific RNA interference strategy aimed at selectively silencing the mutant *MPZ* allele while preserving the wild-type. Candidate siRNA sequences were identified in vitro and are now being tested in dorsal root ganglia myelinating cultures using lentiviral vectors. Ongoing studies aim to validate functional rescue *ex vivo* and *in vivo*.

Overall, this work provides novel mechanistic insight into CMT pathogenesis and establishes a translational framework for mutation-specific therapy. By revealing the developmental nature of CMT1A and advancing allele-specific silencing for CMT1B, this thesis contributes to both fundamental knowledge and therapeutic direction in the field of inherited peripheral neuropathies.

Table of Contents

Introduction

Charcot-Marie-Tooth (CMT) disease is a heterogeneous group of inherited peripheral neuropathies affecting about 1 in 5000 people worldwide and 1 in 3000 in Europe [1,2]. It is classically categorized into three broad subgroups: dys/demyelinating CMT1, characterized by subnormal nerve conduction velocity (NCV) (<35 m/s); axonal CMT2 characterized by normal NCV (45 m/s); and intermediate CMTs characterized by intermediate NCV (35-45 m/s) [3,4]. CMT1 subgroups are further distinguished based on the genetic cause. CMT1A is caused by the duplication of the gene *PMP22* (peripheral myelin protein 22), while CMT1B is caused by mutations of the gene *MPZ* (myelin protein zero) [5].

Despite its significant socio-economic burden, effective therapeutic options for CMT are currently lacking, and its management remains solely supportive and symptomatic. This is mainly due to the fact that our understanding of the molecular mechanisms underlying the majority of CMT subtypes is still incomplete. This work aims at addressing this gap from two complementary perspectives:

(i) We investigated the alterations in early development of myelinated fibers in a rat model of CMT1A and revealed a critical time window in which CMT1A fibers experience a developmental impairment at a structural and molecular level, shedding light on the etiology of this disease.

(ii) We explored the effectiveness of a gene therapy approach based on allele-specific gene silencing for a CMT1B subtype caused by a heterozygous dominant-negative mutation of the *MPZ* gene.

CMT1A

CMT1A is the most common inherited myelin disorder of the peripheral nervous system (PNS), caused by the duplication of a large DNA segment of 1.5 Mb containing the *PMP22* gene. Although the genetic defect has been known for a long time, the pathogenic mechanisms underlying the neurological phenotype are still underexplored [6–8].

Growing evidence supports the dysmyelinating rather than demyelinating nature of CMT1A, albeit developmental myelin and axonal deficiencies as critical features in the pathogenesis of the disease have not been deeply investigated yet [9,10]. CMT1A patients display a remarkable and uniform NCV slowing that does not significantly change throughout their lives. The mean NCV is around 20 m/s and is similar in nerves of both upper and lower limbs and among different patients [8,9,11–13]; moreover, CMT1A patients almost never show temporal dispersion and conduction blocks [12]. This highly preserved electrophysiological picture is rather inconsistent with a typical demyelinating phenotype, which instead occurs in acute and chronic inflammatory demyelinating polyneuropathies [9,11]. Interestingly, the uniform reduction of NCV in CMT1A is detectable starting from the first years of life and is stable for decades with signs of dysmyelination already present in children [12–15]. In this regard, CMT1A electrophysiology also challenges the theory of repetitive de/remyelination, which sometimes has been reported to cause onion bulb formations, in favor of an altered differentiation of Schwann cells (SCs), which likely remain in excess during development [9,12,16,17].

Nerve conduction properties are tightly dependent on geometric parameters of myelinated fibers (MFs); in fact, altered CMT1A neurophysiology reflects pathological nerve abnormalities, including reduced myelin thickness of large fibers, increased myelin thickness of small fibers, and shortened internodes [12,18]. Myelination and specific axon–glial interaction tightly regulate the increase in axonal diameter during development [19–21]. For this reason, it is not surprising that CMT1A peripheral nerves display an altered distribution

of axon populations, with a reduction in larger axons and an increase in smaller ones [19,22–24].

Until now, axonal defects were considered secondary to myelin abnormalities [25]. However, NCV studies and neuropathological evidence support a defect of PNS development in CMT1A likely involving both axon and myelin maturation.

In addition to electrophysiological and neuropathological abnormalities, molecular alterations are also present in CMT1A; among them, an upregulation of markers of immature SCs and a downregulation of lipid metabolism genes have been found in CMT1A rats [22,25]. Consistently, it was recently demonstrated by our lab that the lipid composition of peripheral myelin is also altered in CMT1A [26]. Of note, an impaired myelin lipidome affects nerve fiber architecture and electrophysiological properties. In fact, interfering with lipid biosynthetic pathways improves both neurophysiology and the altered geometric parameters of MFs in CMT1A [25,26].

CMT1B

MPZ encodes the most abundant structural protein of peripheral myelin, and it is necessary for proper myelin formation and compaction [27,28]. *MPZ* mutations account for about 5% of all CMT cases [29,30], and more than 200 pathogenic mutations of this gene have been described. These mutations can be classified into three major subgroups according to the associated clinical manifestation and age of onset [31]:

(i) Hypo/dysmyelinating, including severe and infantile-onset (<6 years old) neuropathies such as Dejerine-Sottas disease (DSS) and congenital hypomyelinating neuropathy type 2 (CHN2), childhood-onset "classical" CMT1B, and late-onset (>40 years old) milder forms of CMT1B.

(ii) Axonal, including late-onset CMT2I/J neuropathies, in which the structure of myelin is relatively intact, but axonal defects are observed.

(iii) Intermediate, including CMTDID neuropathies.

Recently, our group showed that the D61N mutation in the *MPZ* gene, which is associated with a particularly severe and early-onset demyelinating neuropathy with interspersed hypermyelinated fibers in sural nerve biopsy, creates a new glycosylation motif (N-X-S/T), which is absent in the wild-type (WT) protein, resulting in MPZ hyper-glycosylation [32]. Importantly, the same mutation has also been described in a Japanese patient who also presented a severe early-onset demyelinating neuropathy, thus confirming the pathogenicity of this variant [33].

For this reason, a knock-in mouse model carrying the heterozygous MPZ-D61N variant was established using CRISPR-Cas9 ($Mpz^{D61N/WT}$ mice) [34]. Previous work from our lab showed that $Mpz^{D61N/WT}$ mice develop early motor impairment characterized by tremors, which worsen with age. The histological analysis confirmed a dysmyelinating phenotype characterized by diffuse hypomyelination and focal myelin abnormalities reminiscent of the human phenotype [32]. It was also demonstrated that the mutant MPZ protein is hyperglycosylated and trafficked to the myelin membrane, where it impairs proper myelin compaction. Collectively, our data indicate that the $Mpz^{D61N/WT}$ mouse represents an authentic model of severe CMT1B, affirming gain-of-glycosylation in MPZ as a novel pathogenic mechanism of CMT1B disease.

As for CMT1A, management of CMT1B is mostly supportive and symptomatic [35]. Preclinical gene therapy approaches have been tested for CMT1A and for some other CMT forms, such as CMT1X, CMT2A, CMT2D, CMT2S, CMT4C, and CMT4J [36]. Gene therapy for CMT1B presents challenges due to the various pathogenic mechanisms associated

with different mutations, which include both gain-of-function and loss-of-function effects. The level of MPZ expression is also critical; while hyperexpression is detrimental to peripheral myelin, haploinsufficiency leads to a mild neuropathic phenotype [37,38]. Although promising results have been observed with compounds targeting endoplasmic reticulum (ER) stress in the case of ER-retained MPZ variants, it is unlikely that those drugs might effectively cure neuropathies due to MPZ variants that reach the myelin sheath but disrupt the structural integrity of peripheral myelin.

Aims of the Project

Aim I: Overall, data from the literature show that neurophysiological, neuropathological, and molecular alterations are present in CMT1A, but when they arise and become relevant has not been investigated yet. To shed light on pathophysiological mechanisms that occur during development and to investigate the relationship among axonal, myelin, and lipidome deficiencies in CMT1A, we extensively analyzed the evolution of both myelin lipid profile and MF structure in WT and CMT1A rats. We found that CMT1A peripheral nerves display an immature phenotype, characterized by a highly consistent maturation delay in both myelin lipidome and axon-related morphometric parameters.

Aim II: In parallel, we decided to exploit the *Mpz*$^{D61N/WT}$ mouse model to test a silencing siRNA approach to reduce the mutant D61N protein expression without affecting WT MPZ levels. This strategy could provide the proof-of-principle for a therapeutic method that transforms a severe MPZ-related gain-of-function demyelinating neuropathy into a milder haploinsufficiency phenotype.

Materials and Methods

Animal Models

The CMT1A rat has been developed in the K.-A. Nave laboratory by overexpressing the WT murine *Pmp22* gene [39]. Heterozygous CMT1A animals and WT littermates of both sexes at postnatal day (P) 5, P10, P15, P20, P30, P60, P75, P180, and P365 were used for all the experiments.

The CMT1B mouse was generated in collaboration with the San Raffaele Institute in Milan, as described elsewhere [34].

PNS Myelin Isolation

Sciatic nerves from P5, P10, P20, P30, P60, and P180 rats were used to prepare myelin-enriched fractions as previously described [40,41]. We analyzed WT (n = 7) and CMT1A (n = 7) samples for each time point. To obtain a sufficient amount of purified myelin at P5, eight sciatic nerves from four different rats of the same sex and genotype were pulled together for each sample; for P10 and P20 myelin samples we used four nerves from two rats of the same sex and genotype; for P30 myelin samples we used two nerves from one rat; for P60 and P180 myelin samples, one nerve was used. Both male and female animals were included at each time point.

Lipid Extraction

Samples were added with 1 mL of IPA (previously added with 1 mL/mL of SPLASH® Lipidomics® Mass Spec Standard), incubated for 15 min on a shaker at room temperature, and then sonicated in ice-cold water for 10 min. After that, the suspension was centrifuged at 20,000 *g* for 20 min at 4°C. The supernatant was then transferred into a new tube. The pellet was re-extracted with 100 mL of methanol: MTBE (1:1, *v*/*v*), incubated for 15 min on a shaker, and centrifuged at 20,000 *g* for 20 min at 4 °C. The supernatant was then pooled with the one collected in the previous extraction and dried under a nitrogen stream. Concentrated samples were resuspended with 50 µL of methanol: chloroform (9:1, *v*/*v*) for untargeted liquid chromatography with tandem mass spectrometry (LC-MS/MS) analyses. Samples were randomized and split into four different batches. Each batch included a consistent number of quality control (QC) samples (extracted from commercial mouse plasma), that were used to re-align and normalize data derived from different batches.

Untargeted LC-MS/MS Analyses

The lipidomic analyses were carried out on an ACQUITY UPLC system coupled to a Synapt G2 QToF high-resolution mass spectrometer (Waters, Milford, MA, USA), acquiring both in positive (ESI+) and negative (ESI−) ion modes.

Lipids were separated on a reversed-phase CSH C18 column (2.1×50 mm, 1.7 µm), whose temperature was kept at 50 °C and eluted at a flow rate of 0.450 mL/min using the eluents: A = 10 mM ammonium formate in acetonitrile/water (60:40 *v*/*v*), B = 10 mM ammonium formate in isopropyl alcohol/acetonitrile (90:10 *v*/*v*). The gradient was the following: 0.0–1.0 min 10% B, 1.0–4.0 min 10 to 60% B, 4.0–8.0 min 60 to 75% B, 8.0–9.5 75 to 100% B and kept for 1.5 min. Then the column was reconditioned at 10% B for 2 min. The total run time was 13 minutes and the injection volume was set to 3 µL and 5 µL for acquisition in ESI+ and ESI−, respectively.

The scan range was set from 50–1200 m/z. Cone voltage was set at 35 V. Source temperature was set to 90 °C, desolvation temperature was set to 400 °C, and desolvation gas and cone gas (N_2) flows were set to 600 and 30 L/h, respectively. The scan time was set to 0.3

s, low collision energy was set to 4 eV. Leucine enkephalin (2 ng/mL) was infused as lock mass for real-time spectra recalibration. MassLynx software version 4.1 (Waters) was used for data acquisition.

Features were extracted from raw data using TargetLynx software version 4.1 (Waters). Features with a signal-to-noise ratio below 10 were removed. Features with more than 50% of missing values and features with RSD (relative standard deviation) > 25% in the QC samples were removed. For the principal component analysis and heatmap visualization, data were log transformed and Pareto scaled.

Quantitative Neuropathology on Sciatic Nerves During Development

Morphological and morphometric studies were carried out on sciatic nerves from P5, P10, P15, P20, P30, P75, P180, and P365 WT (n = 3 for each time point) and CMT1A (n = 3 for each time point) rats fixed in 2.5% glutaraldehyde in cacodylate buffer and embedded in Epon. Semithin sections (0.8 μm) were cut, stained with toluidine blue, and photographed at a 1000× magnification with an Olympus PROVIS AX60 microscope connected to a JVC digital camera. Morphometric evaluation was performed using a custom macro based on the Image Pro-Plus Software version 7.0 (Immagini e Computer, Rho, Milan, Italy), which was able to extract nine different morphometric parameters from digitized images. For each MF, the fiber perimeter and axon perimeters were traced, automatically obtaining the respective areas; fiber and axon diameters were derived from a circle of the corresponding area. The G-Ratio (axon diameter/fiber diameter) was calculated and plotted as a function of axon diameter; fiber density and roundness (defined as π × diameter/perimeter) were also measured. Fibers associated with "hyperintense" cells (cells appearing dark blue following toluidine blue staining) were manually excluded, since they were not correctly segmented by our macro. Average values were obtained for all parameters for the two genotypes at each time point. Fiber Roundness was defined as π × diameter/perimeter. This parameter can be used as a parameter of tissue integrity since it is sensitive to physiological strains acting on myelinated fibers during development; for the same reason, it is a useful criterion to exclude from the analyses fibers displaying artifacts due to tissue processing.

At P5, at least 1000 MFs were evaluated for each rat; at later time points, at least 3000 MFs were evaluated for each rat, for a total of about 130,000 MFs.

For transmission electron microscopy analysis, 70 nm ultra-thin sections were cut and stained with 1% uranyl acetate and lead citrate solution. Images were collected with a Jeol JEM 1011 (Jeol, Japan) electron microscope, operating with a maximum acceleration voltage of 100 kV, and recorded with a 2 Mp charge-coupled device camera (Gatan Orius SC100).

Plasmids and siRNAs

The plasmids carrying MPZ-D61N and MPZ-D61N, and the shRNA lentiviral vectors were synthesized by VectorBuilder. The 19 siRNA sequences were synthesized by Eurofins Genomics. The lentiviral packaging plasmids (pMDLg/pRRE, pRSV-Rev, and pMD2.G) were a gift from Didier Trono (Addgene plasmids #12251, #12253, and #12259) [42]

In vitro siRNA Screening

HeLa cells were grown in DMEM (Gibco, #11965092) supplemented with 10% FBS (Gibco, #A5256701) and 2 mM L-Glutamine (Gibco, #A2916801) in a humidified incubator at 37°C and 5% CO2.

For the quantification of fluorescence intensity, transfections were performed using Lipofectamine 3000 (ThermoFisher, Cat#L3000001) following the manufacturer's protocol. Specifically, cells were plated on a 96-well cell culture plate (BioFil, #TCP011024) to ensure

about 80% confluency at the time of transfection; 0.2 µg of MPZ-WT plasmid, 0.2 µg of MPZ-D61N plasmid, and 0.3 µL of Lipofectamine were added to each well, together with different amounts of siRNAs. Cells were imaged 48h after transfection using the Incucyte SX5 live-cell analysis system with a 20x objective. The mean red and green fluorescence intensity was measured using Fiji software [43] and averaged for at least two separate wells. Three independent replicate experiments were performed.

For Western Blot quantification, cells were lysed 48 hours after transfection in 40 uL of RIPA buffer (NaCl 150 mM, Triton X-100 1%, sodium deoxycholate 0.5%, SDS 0.1%, Tris-HCl 50 mM in deionized water, pH adjusted to 7.4) supplemented with NaF to a final concentration of 5 mM, $NaVO_4$ to a final concentration of 1 mM, Phenylmethylsulfonyl fluoride to a final concentration of 1 mM, and phosphatase and protease inhibitor cocktail (Merck P8340, used 1:100). Cell lysates were diluted in Laemmli buffer (Tris 62 mM, SDS 8%, glycerol 10%, bromophenol blue 0.1%, 2-mercapto-ethanol 5%) and loaded into 4–15% Mini-PROTEAN® TGX Stain-Free™ Protein Gels (BioRad, #4568084). Gel was activated using a BioRad Chemidoc MP Imager and then transferred onto a PVDF membrane (BioRad, 1620177). After blotting, the membrane was imaged using the Chemidoc Imager to quantify total protein content for each lane and blocked with 5% BSA in TBST for 1h at room temperature. Then, the membrane was incubated with the ant-MPZ primary antibody (Abcam #ab31851, used 1:5000 in TBST) overnight at 4°C. After washing with TBST, the membrane was incubated with the HRP-conjugated secondary antibody (Santa-Cruz, #sc-2357, used 1:5000) for 90 minutes at room temperature, and then washed again with TBST. Finally, the membrane was imaged using BioRad Chemidoc MP Imager after incubation for 5 minutes with Clarity™ Western ECL Substrate (BioRad, #1705060). Densitometric quantification was performed using the BioRad Image Lab software (v. 6.1.0).

DRG Cultures Preparation

Dorsal root ganglia (DRG) cultures were prepared as described elsewhere [26,44]. Specifically, WT females were mated with *Mpz*$^{D61N/WT}$ males (or vice versa) and inspected daily for the presence of a vaginal plug. Pregnant dams were euthanized at gestational day 14 (considering day 0 as the day the vaginal plug was found). After collecting the embryos, the DRGs were dissected and incubated in a solution containing 0.25% Trypsin for 1 hour in the incubator. DRGs were then centrifuged to remove trypsin, washed two times with L-15 medium (Gibco, #11415064) supplemented with FBS 10% (Gibco, #A5256701), and resuspended in C-Medium [MEM (Gibco, #11095080) supplemented with FBS 10% and NGF (Gibco, #13257-019) 10 ng/mL]. Then, they were triturated by pipetting, and DRG cells were plated in 24-well plates at a density of 36000 cells/well. Twenty-four hours after plating, the culture medium was changed in Neurobasal (Gibco, #21103049) supplemented with B-27 (Gibco, #17504044), and lentiviral vectors were added to the culture medium to transduce DRG cells. Five days after seeding, the culture medium was changed again to C-Medium supplemented with ascorbic acid 50 ng/mL (Gibco, # 011188.22) to induce myelination. After 2 additional weeks, cultures were lysed in RIPA buffer for Western blot or fixed in paraformaldehyde 4% in PBS for immunohistochemistry.

Lentiviral Vectors Preparation

To prepare lentiviral vectors, HEK293T cells (ATCC #CRL-3216) were grown in DMEM (Gibco, #11965092) supplemented with FBS 10% (Gibco, #A5256701), and L-Glutamine 2 mM (#Gibco, #2916801); The day before transfection, cells were plated in 10 cm Petri dishes ($4x10^6$ cells/dish); The day of transfection, the culture medium was replaced with DMEM supplemented with L-Glutamine 2 mM (without FBS), and 4 h later cells were transfected using Calcium Phosphate Precipitation. First, a solution was prepared containing 26 µg/ml of

transfer vector, 26 µg/ml of pMDLg/pRRE plasmid, 6 µg/ml of pRSV-Rev plasmid, 6 µg/ml of pMD2.G plasmid, and 250 mM CaCl2 in deionized water; then, this solution was added dropwise to an equal volume of HBS buffer (NaCl 270 mM, KCl 20 mM, NaHPO4 1 mM, HEPES 42 mM, Glucose 0.2%), while bubbling air into the HBS buffer using an automatic pipette controller. After incubation at room temperature for 25 minutes, 1 mL of the final DNA/Calcium Phosphate solution was added dropwise to each 10 cm dish.

Statistical Analysis and Data Visualization

To choose the appropriate statistical test, Shapiro–Wilk and Kolmogorov–Smirnov tests were used to test for normality, and an F test was used to test for equality of variance. For the comparison of morphometric parameters, one-way ANOVA was performed, followed by Sidak's multiple comparison test; For the comparison of G-Ratios, a Kruskal-Wallis test was performed, followed by Dunn's multiple comparison test. The threshold for statistical significance was set at $p < 0.05$. For each experiment, the statistical test used is reported in the figure legends. Lipid enrichment analysis was performed using the LION web tool (LION/web|Lipid Ontology enrichment analysis) [45,46].

GraphPad Prism software version 9 (GraphPad Software Inc., San Diego, CA, USA) was used to perform all the statistical comparisons and to generate most of the graphs. The R packages factoextra (v. 1.0.7) (CRAN—Package factoextra (r-project.org) and ggplot2 (v. 3.4.4) (CRAN—Package ggplot2 (r-project.org) were used to generate the principal component analysis (PCA) plots of lipidomic data and the axon diameter frequency density plots. The heatmap of lipidomic data was generated using MetaboAnalyst (https://www.metaboanalyst.ca/MetaboAnalyst/, version 6.0). Network visualization of lipid metabolism was generated using Cytoscape (v. 3.10.1) (https://cytoscape.org/).

All figures were prepared using Adobe Illustrator 2023 (Adobe, San Jose, CA, USA).

Results I

Maturation of Myelin Lipid Composition is Delayed in CMT1A

Our lab recently demonstrated that the lipid composition and structure of peripheral myelin are altered in adult CMT1A rats [26]. Whether this alteration is due to impaired myelin maturation or a maladaptive response to chronic nerve damage during disease progression remains to be proven. To address this issue, we first monitored the lipid profile of WT and CMT1A myelin during development from P5 to P180 using high-resolution liquid chromatography with tandem mass spectrometry (LC-MS/MS).

The PCA score plots of lipidomic data show that, in both WT and transgenic rats, myelin lipid composition changes over time, indicating a continuous maturation process (**Figure 1a** and **Supplementary Figure 1a**). CMT1A and WT myelin are mostly similar in the first ten days after birth. However, from P20 onwards, CMT1A myelin significantly diverges from the WT (**Figure 1b, c**). Consistently, when P5-P180 CMT1A lipid profiles are individually plotted together with the WT, starting from P20, they were shifted towards earlier developmental stages (**Supplementary Figure 1b**). Interestingly, we found that P20 CMT1A myelin is characterized by a marked decrease in almost every sphingomyelin (SM) and hexosylceramide (HexCer) species compared to WT (**Supplementary Figure 1c**), together with an increase in acylcarnitines (CAR) and some glycerophospholipid (GPL) species (**Supplementary Figure 1c**). Several SM species show a decrease in CMT1A myelin already at P5 and P10 (**Supplementary Figure 2a, b**), indicating that myelin abnormalities, even if subtler, are already present at an early postnatal age. To gain knowledge about this developmental impairment, we defined lipid groups based on the trajectory pattern of their

levels (**Figure 1d, e**). We identified two groups displaying a significant difference between WT and CMT1A myelin: group A, consisting of HexCers and long-chain SMs, whose concentration markedly increases in WT but not in CMT1A myelin; and group B, including a subgroup of phosphatidylcholines (PC) and phosphatidylethanolamines (PE), whose concentration decreases during development but remains significantly higher in CMT1A (**Figure 1d**). We also identified two additional groups displaying a similar developmental trajectory in the two genotypes: group C, consisting of long-chain poly-unsaturated triglycerides (TG), whose concentration increases during development; and group D, including other subgroups of PC and PE, whose concentration decreases during development (**Figure 1d**).

To further investigate the biological significance of these results, we performed a lipid ontology search on the four groups. Interestingly, group A was significantly enriched in saturated and mono-unsaturated very long-chain fatty acids (C22–24), whilst group B was enriched in short-chain fatty acids (**Figure 1e)**. Finally, group C and group D were enriched in triacylglycerols and unsaturated short- and medium-chain fatty acids (C18 and C20), respectively (**Supplementary Figure 3**).

Overall, lipidomic profiling revealed a delayed maturation of CMT1A myelin already detectable at P10, which becomes substantial at P20. In particular, CMT1A myelin is deprived of lipid species that are deemed important to guarantee optimal structural and electrophysiological properties, while displaying higher levels of lipids typical of unspecialized plasma membranes [47,49,50].

Maturation of Myelinated Fibers Structure is Delayed in CMT1A

We then paralleled lipidomic data with an extensive quantitative neuropathology study from P5 to P365, to pinpoint at which developmental stage the morphological alterations arise. We analyzed nine different geometric parameters of over 130.000 fibers, using an ad hoc semi-automated image analysis algorithm based on the Image Pro-Plus Software (v. 7.0; Immagini e Computer, Rho, Milan, Italy), previously developed in our lab (see Materials and Methods for details).

We found that, from P15–P20 onwards, CMT1A nerves display reduced axon and fiber diameter (**Figure 2a, b**). Moreover, the myelinated area is lower in CMT1A compared to WT (**Figure 2b**), while fiber density and roundness are not affected by any relevant change (**Supplementary Figure 4a, b**). We also identified and quantified a subset of myelinating SCs that we called “hyperintense cells” due to their dark-blue appearance in toluidine blue-stained sections. The number of these cells is high at early developmental stages (P5), and decreases over time, albeit to a lesser extent in CMT1A than in WT nerves (**Supplementary Figure 4c, d**). Electron microscopy micrographs showed that “hyperintense cells” are characterized by an extensive endoplasmic reticulum network (**Supplementary Figure 4e)**, a typical feature of cells characterized by high protein and lipid biosynthesis [51,52].

Given that axonal diameter and myelin thickness increase during physiological development and deeply influence nerve conduction velocity, we further examined these parameters in WT and mutant animals. First, to characterize axonal growth, we analyzed the axon diameter frequency distribution at each time point. The results show that, in WT animals, the frequency distribution steadily shifts towards larger caliber axons until P180, and then stabilizes (**Figure 3a**). Instead, in CMT1A animals, the frequency distribution remains stable until P20, and then displays just a small shift between P30 and P365 (**Figure 3a**).

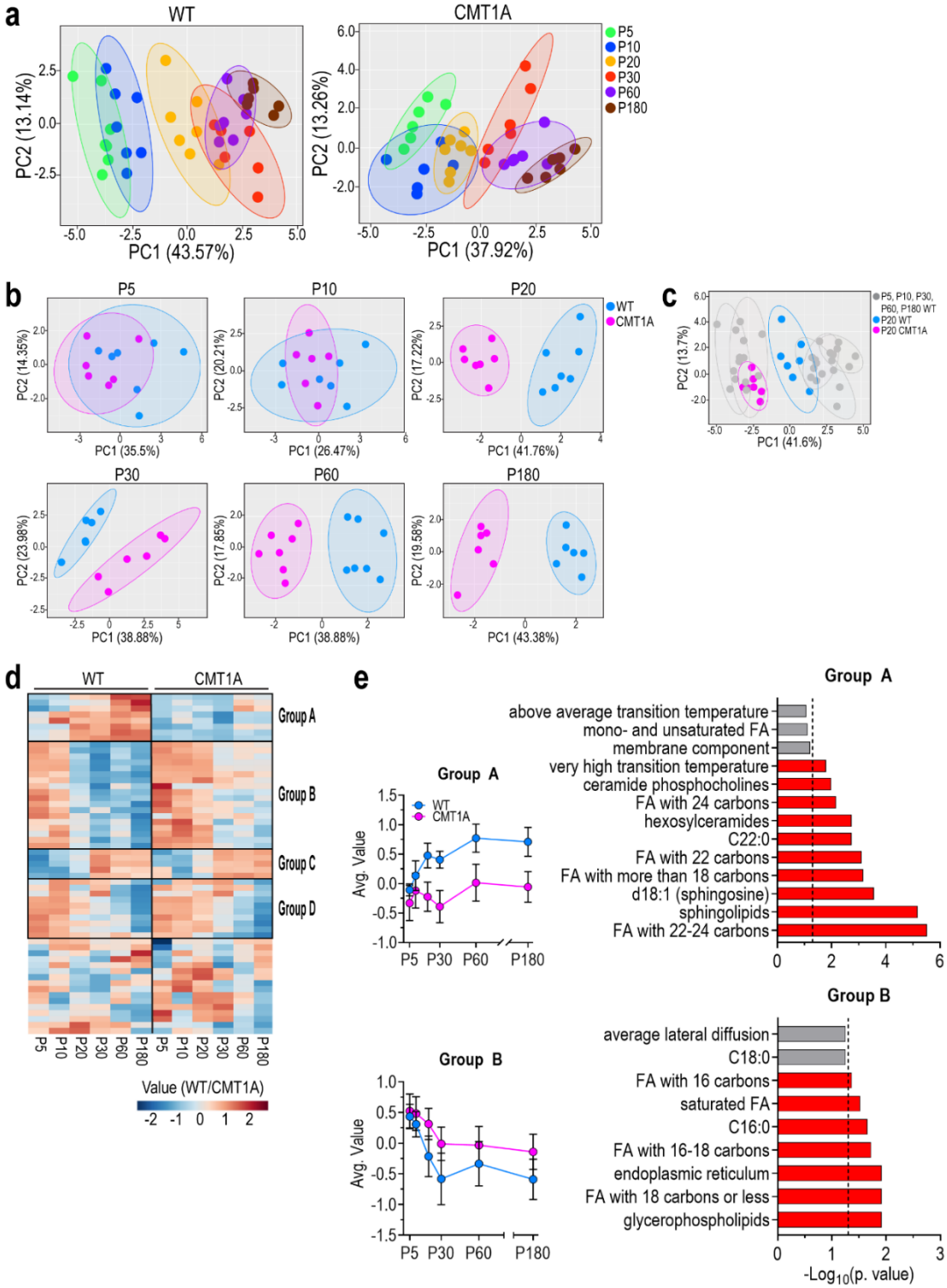

Figure 1. Impaired maturation of peripheral myelin lipid composition in CMT1A rats. (**a**) PCA plot of lipidomic data from WT (left) and CMT1A (right) purified peripheral myelin isolated from the sciatic nerve of P5, P10, P20, P30, P60, and P180 rats. n = at least 6 samples for each group. (**b**) Same data as in **a**, but WT and CMT1A samples at the same time point are plotted together in the same PCA plot (**c**). Same data as in **a**, but CMT1A P20 samples are plotted together with WT samples, to highlight the maturation delay experienced by CMT1A myelin at this time point. (**d**) Heatmap of lipidomic data. The four black rectangles highlight groups of lipids with a similar developmental trajectory. (**e**) On the left, average value of lipids in group A (top) and group B (bottom); on the right, results of enrichment analysis performed using LION software version 2023.04.14 on lipids in group A (top) and group B (bottom). The dotted line marks the p value significance threshold (0.05).

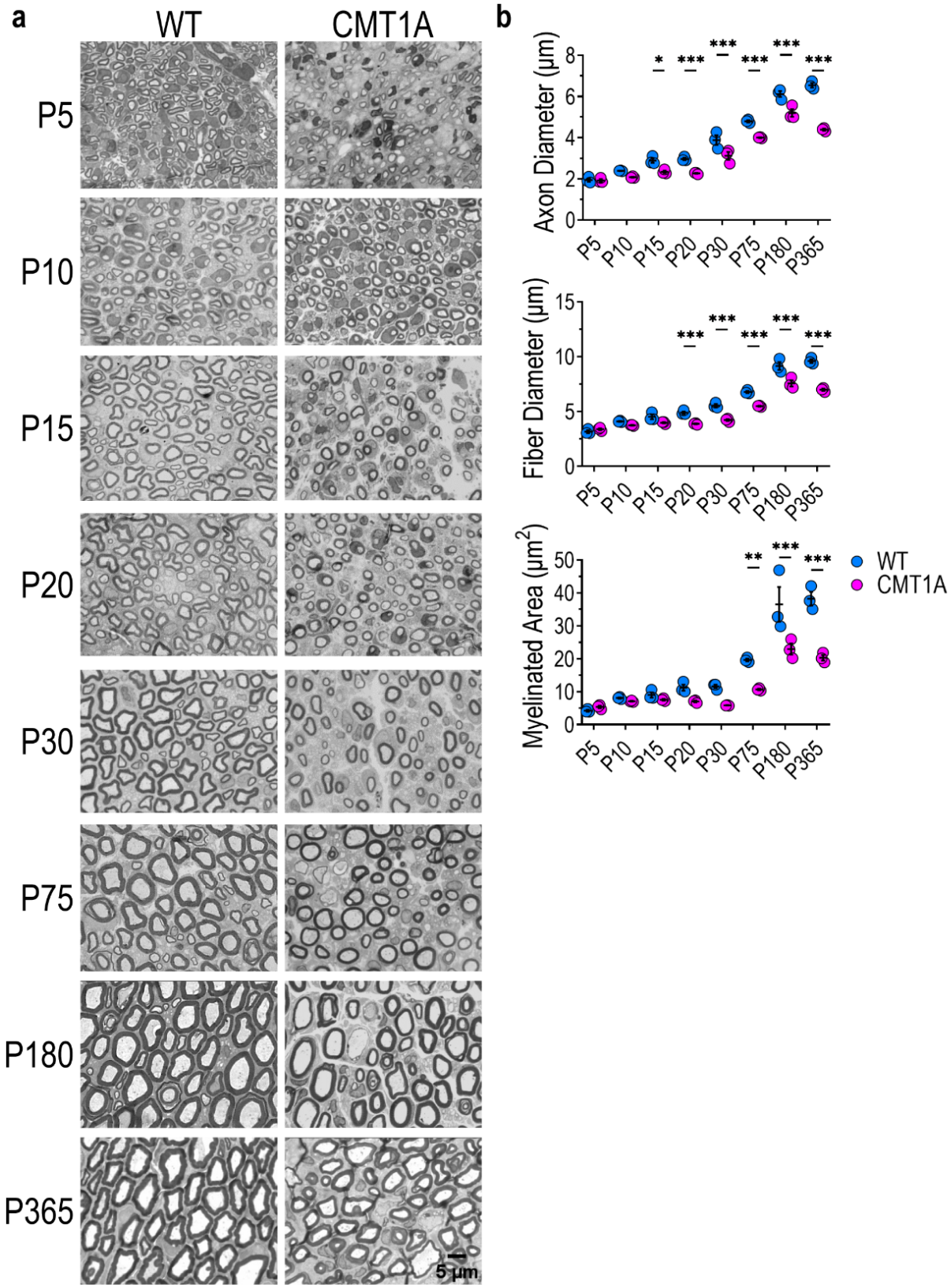

Figure 2. CMT1A myelinated fibers display impaired postnatal architectural development. (**a**) Micrographs of cross-sections of WT and CMT1A sciatic nerves at P5, P10, P15, P20, P30, P75, P180, and P365, stained with toluidine blue. Scale bar: 5 µm. (**b**) Morphometric parameters from WT and CMT1A sciatic nerve sections. n = 3 rats for each genotype and each time point. At P5, at least 800 myelinated fibers were evaluated for each rat; at later time points, at least 3000 fibers were evaluated for each rat. Values are presented as mean ± SEM. *: $p < 0.05$, **: $p < 0.01$, ***: $p < 0.001$. p values were calculated using one-way ANOVA followed by Sidak's multiple comparisons test between the two genotypes at each time point.

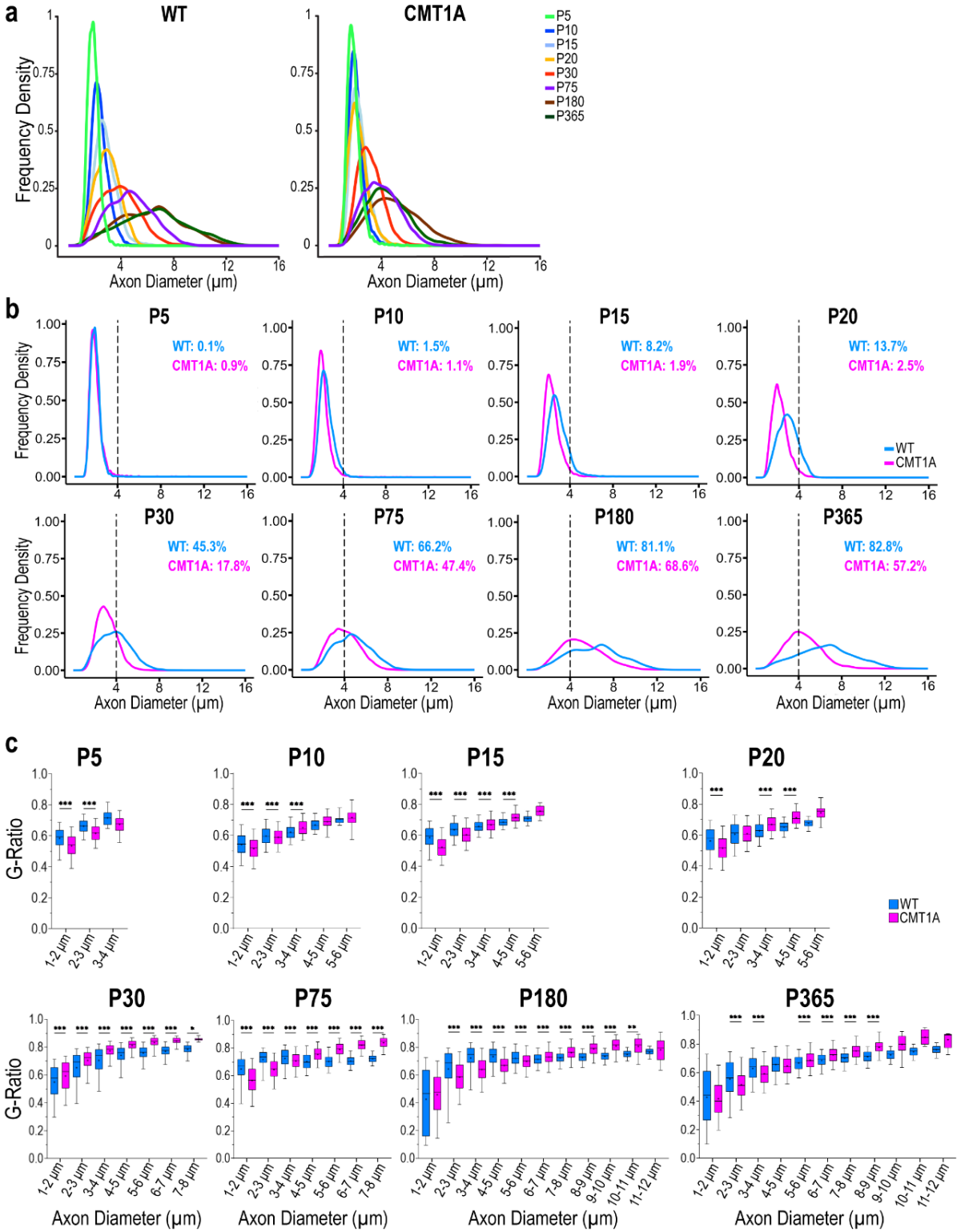

Figure 3. CMT1A myelinated fibers display impaired axon growth and aberrant myelination. (**a**) Frequency distribution of axon diameters in WT (left) and CMT1A (right) sciatic nerves at different developmental stages. (**b**) Same data as in **a**, but the frequency distributions of WT and CMT1A axons at the same time point are plotted together. The dotted line marks the 4 µm threshold. The fraction of fibers with an axon diameter larger than 4 µm is reported in each graph. (**c**) Boxplots of the G-Ratio for each fiber class in WT and CMT1A rats at different developmental stages. For P5 animals, 3000 myelinated fibers from three different animals per genotype were evaluated; for later time points, 9000 myelinated fibers from three different animals per genotype were evaluated. The dot inside each box represents the mean. *: $p < 0.05$, **: $p < 0.01$, ***: $p < 0.001$. p values were calculated using the Kruskal-Wallis test followed by Sidak's multiple comparisons test between the two genotypes for each axon diameter class.

Overall, these data indicate that axonal growth in CMT1A animals is severely impaired and delayed compared to the WT; as a result, juvenile and adult CMT1A nerves show a progressive accumulation of small-caliber fibers and a concomitant deprivation of large-caliber ones (**Figure 3b**). As an example, at P180 and P365, the percentage of fibers with an axon diameter larger than 4 μm (which we assumed as a threshold to divide small- from medium/large-caliber axons) was above 80% in WT nerves, while it was below 60% in CMT1A nerves (**Figure 3b**).

Then, in order to monitor myelin development and characterize the growth of the myelin sheath, we analyzed the average G-Ratio of WT and CMT1A fibers, following their grouping based on axonal diameter. This grouping is crucial for the correct description and interpretation of the results; in fact, since G-Ratio strongly depends on axon caliber (**Supplementary Figure 5a**), only G-Ratios measured from axons of the same size and at the same developmental stage can be meaningfully compared. We found signs of hypo- (increased G-Ratio) and hyper-myelination (decreased G-Ratio) in CMT1A fibers already at P10 (**Figure 3c** and **Supplementary Figure 5b**). In particular, the largest fibers are significantly reduced and hypo-myelinated in CMT1A compared to the WT at each time point, while the smallest fibers are increased and hyper-myelinated (**Figure 3c)**. Interestingly, small/medium-caliber fibers (2-5 μm of axon diameter), which are the largest fibers at early time points and the smallest at later stages, are hypo-myelinated in young CMT1A nerves, but become hyper-myelinated at later stages (**Supplementary Figure 5c**). This result suggests that myelination in CMT1A nerves progresses at a different pace than in the WT nerves and that it possibly also occurs in a shifted time window. Overall, this evidence indicates that axonal growth is delayed and defective in CMT1A; consequently, CMT1A nerves display an accumulation of small-caliber fibers, which are also hyper-myelinated.

Results II

Identification of siRNA Sequences That Can Selectively Silence the Mutant *MPZ* Allele *in vitro*

To assess allele-specific gene silencing as a therapeutic strategy in our $Mpz^{D61N/WT}$ mouse model, we first wanted to identify a siRNA sequence that could selectively target the mutant MPZ-D61N allele over the WT. To do this, we screened all possible 21 base pair-long siRNA sequences targeting the region of the *MPZ* mRNA containing the mutant nucleotide (**Figure 4a**), using a double fluorescence reporter assay. Specifically, we transfected HeLa cells with two plasmids, one carrying the mutant MPZ protein conjugated with EGFP and one carrying the WT MPZ conjugated with mCherry, together with one of the siRNAs. Two days after transfection, we evaluated fluorescence intensity as a readout for silencing efficiency. The results showed that several siRNA sequences showed effective and specific silencing (**Figure 4b**, **Supplementary Figure 6**). For the seven most promising siRNA sequences, silencing was also confirmed using Western blot (**Figure 4c**). We selected for the following experimental step the three sequences showing the most effective silencing of MPZ-D61N protein (>80% reduction of the protein level) and the lowest effect on the MPZ-WT protein (<20% reduction of the protein level).

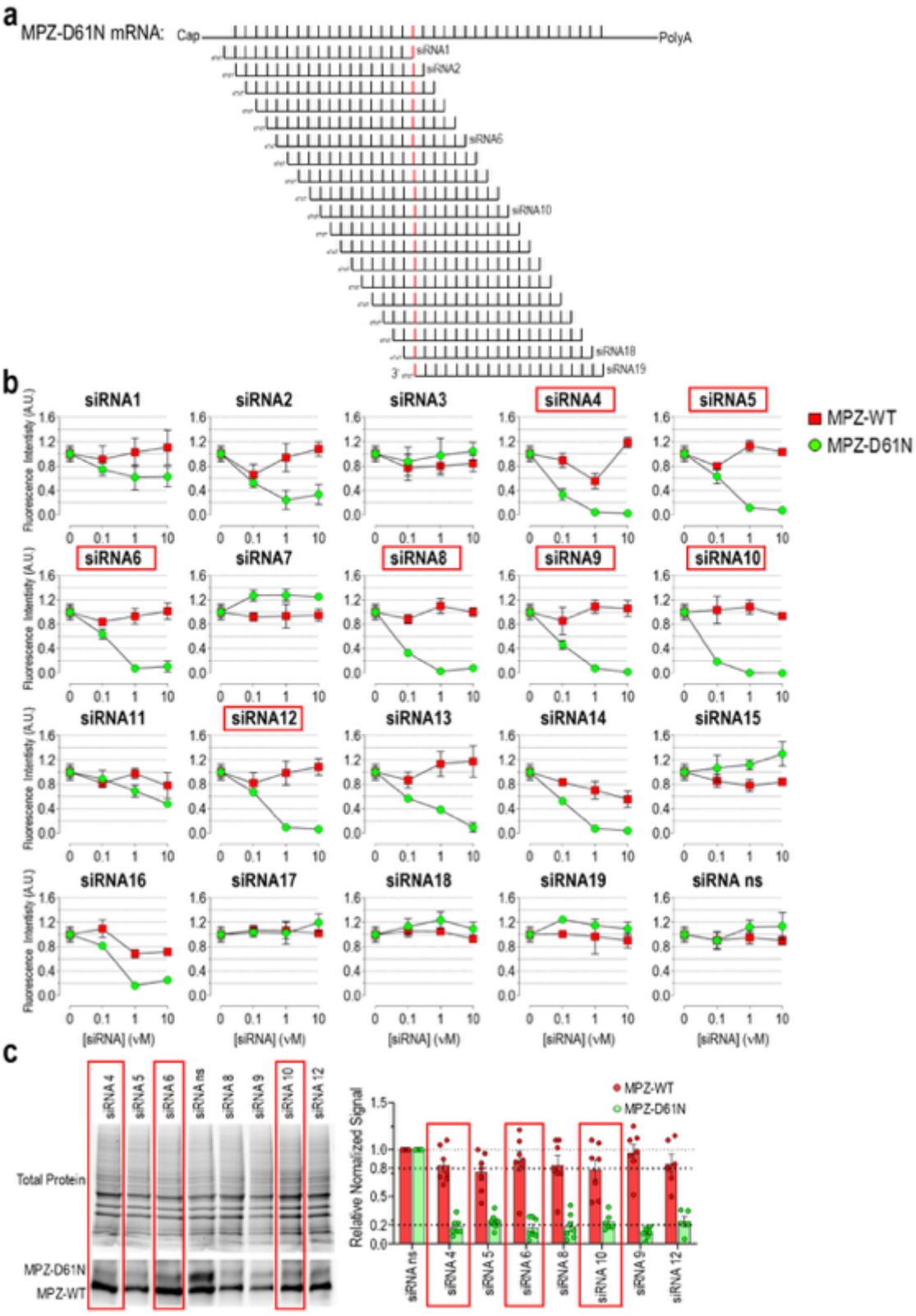

Figure 4. *In vitro* siRNA screening. (**a**) Schematic representation of the 19 siRNA sequences tested in this study. The mutant nucleotide is highlighted in red. (**b**) Results of the double fluorescence reporter assay for each of the19 siRNA sequences tested and for the non-specific control (siRNA ns). The red box highlights siRNA sequences showing the most promising activity. (**c**) Western Blot (left) and relative densitometric quantification (right) on HeLa cells transfected with MPZ-WT, MPZ-D61N, and one siRNA. The most promising candidate sequences are highlighted by the red rectangles.

Testing siRNA Sequences *ex vivo*

To test these sequences in a more physiological setting, we decided to deliver them to dorsal root ganglia (DRG) myelinating cultures using lentiviral shRNA-expressing vectors. It has already been demonstrated that DRG cultures prepared from *MPZ*$^{D61N/WT}$ embryos show myelin abnormalities reminiscent of the so-called focal hypermyelination observed *in vivo* [34, also see **Supplementary Figure 7**]. For this reason, we hypothesized that transducing mutant DRG cultures with lentiviral shRNA-expressing vectors carrying the siRNA sequences selected in the previous step would result in the reduction of myelin abnormalities.

First, we confirmed, using DRG cultures prepared from WT embryos, that we were able to infect myelinating Schwann cells with good efficiency (>70%) (**Figure 5**).

We are now in the process of preparing DRG cultures from *MPZ*$^{D61N/WT}$ embryos. We will then infect these cultures with three different lentiviral shRNA-expressing vectors, each carrying one of the siRNA sequences. Then, we will validate the silencing efficiency and specificity of each sequence via Western blot, and finally we will determine which sequence will result in the most effective rescue of the dysmyelinating phenotype. To do this, we will evaluate several morphological parameters of DRG cultures, including internode length and diameter, and the density of myelin abnormalities.

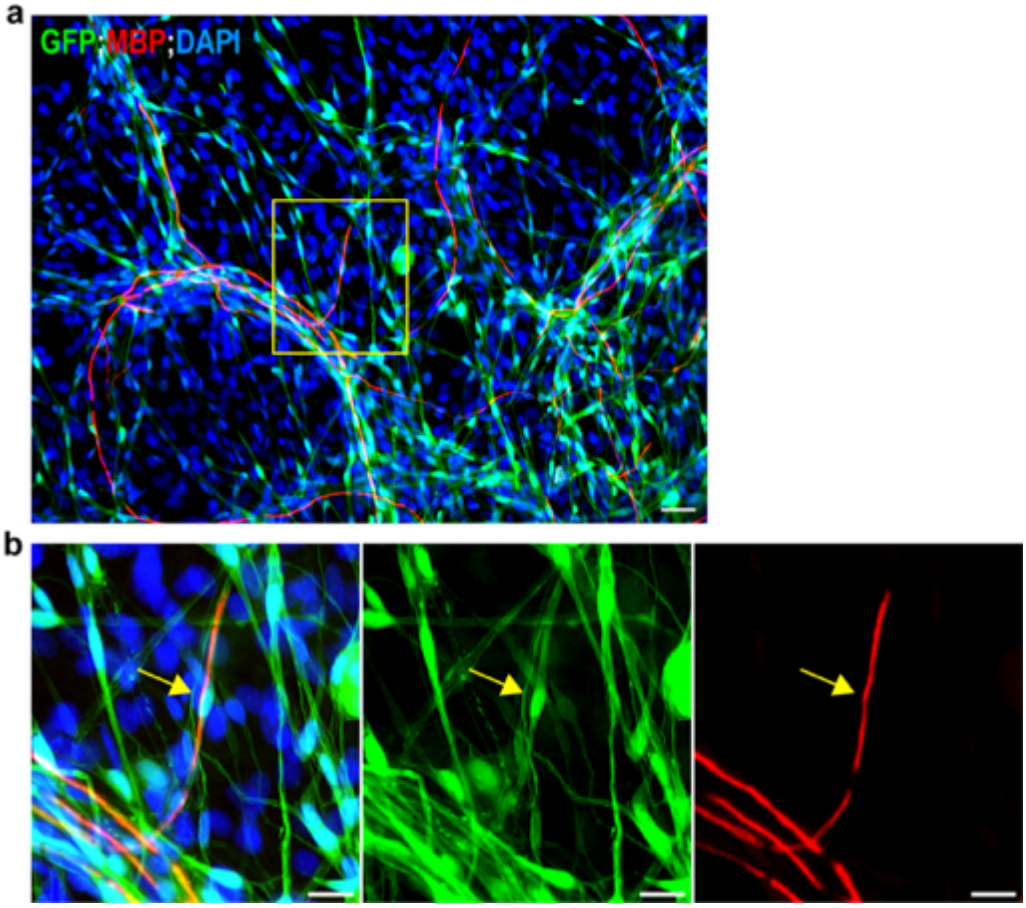

Figure 5. Schwann cells transduction efficiency in DRG cultures. (**a**) Immunofluorescent staining of WT DRG culture transduced with a lentiviral vector for GFP expression (green) after three weeks in vitro. Cultures were immunostained for MBP (red) and counterstained with DAPI (blue). Scale bar: 20 µm. (**b**) Zoomed images of the region highlighted by the yellow rectangle in **a**. Scale bar: 10 µm. The yellow arrows indicate a GFP-expressing myelinating Schwann cell.

Discussion

This thesis addresses the two main research goals of our laboratory: elucidating the molecular mechanisms underlying CMT1 neuropathies, a prerequisite for the development of effective therapies, and exploring novel therapeutic strategies for these disorders.

Although both CMT1A and CMT1B arise from genetic defects affecting structural proteins of peripheral myelin and ultimately lead to altered myelination in the PNS, they are characterized by markedly distinct clinical and pathological phenotypes. This divergence likely reflects profound differences in the underlying molecular mechanisms and suggests that these conditions require tailored therapeutic approaches rather than a uniform treatment strategy.

Several studies support the potential efficacy of gene therapy for CMT1A [53–55]. However, when considering the inherent risks associated with gene therapy and the relatively preserved quality of life of most CMT1A patients, despite chronic neuropathic symptoms such as muscle weakness, the feasibility of such an approach warrants careful evaluation. In contrast, for severe forms of CMT1B, including those caused by the MPZ-D61N mutation, the risk–benefit balance appears more favorable, as the severity of the disease may justify more aggressive therapeutic interventions.

In the first part of this work, we monitored the maturation of peripheral myelin lipid composition in WT and CMT1A rats, and we highlighted an early developmental impairment of CMT1A myelin. Moreover, we analyzed the evolution of morphological parameters in MFs and found that CMT1A axons and myelin sheaths display defective growth, starting soon after birth.

Myelination is a complex and finely regulated process that begins during the early stages of development in mammals and gives rise to long-lasting membrane structures [56–58]. In particular, the maturation of human PNS begins during early intrauterine life: NCV steadily increases between 24 and 40 weeks of gestation, reaching values of 20–25 m/s at birth [59], and approaching adult values (50–60 m/s) at 2–4 years of age, concomitantly with the anatomical maturation of peripheral nerves and the increased motor skills of the child [60,61]. In line with that, the structural maturation of peripheral nerves consists of a doubling in axonal diameter between 5 months and 4 years, an increase of myelin thickness in the first 4–5 years, and an elongation of internodes until the second decade of life by more than a factor of 4 [60–62].

CMT1A patients display a remarkable, uniform, and persistent NCV slowing (20 m/s) by the age of 2 years [8,9,11–13]; moreover, CMT1A sensory and motor nerves show structural abnormalities, including reduced myelin thickness, shortening of internodal length, loss of large-diameter fibers, and onion bulb appearances [13,63]. Interestingly, CMT1A children under 1 year old have normal or almost normal NCV and structural organization of peripheral nerves comparable to healthy subjects of the same age [63,64]. Therefore, NCV studies and neuropathological evidence support the hypothesis of defective PNS development in CMT1A, likely involving both axon and myelin maturation.

To date, chemical features of myelin during PNS development have been poorly investigated compared with the central nervous system (CNS), and available studies mainly focus on adult animals or aging processes analyzed by transcriptomic or proteomic analyses [65–70].

We analyzed the whole lipidome of peripheral myelin in WT and CMT1A rats during PNS development. This allowed us to characterize for the first time the evolution of lipid composition of WT peripheral myelin and to shed light on crucial aspects of CMT1A etiopathology.

We selected key time points to cover the temporal window of PNS development. Indeed, at birth, the fibers of peripheral nerves are almost devoid of myelin, and neurophysiological studies demonstrated that the NCV of the sciatic nerve in rats rapidly increases during the first three postnatal weeks, becoming 16 times faster than at birth and stabilizing later at P40–60 [71–73].

The results obtained from the lipidomic profiling show that PNS myelin in WT rats changes during development, shifting from a composition typical of unspecialized biological membranes to that of a specialized multilamellar myelin membrane. In particular, we observed an enrichment in very long-chain sphingolipids, as already demonstrated at the peak of myelination in the CNS of normal postnatal rats [66,74,75].

Transcriptomics data showed that CMT1A SCs fail to mount an adequate lipid biosynthetic program during development [25]. Our data corroborate this finding and are consistent with our previous results [26], highlighting that this impairment does not just rely on lipid shortage but rather on the delayed maturation of peripheral myelin composition in CMT1A. Although some alterations in CMT1A myelin are already present at P5, the difference between WT and CMT1A myelin lipid profiles becomes relevant between P10 and P20, concomitant with the myelination peak. This is not surprising, as defects in lipid metabolic pathways are exacerbated by the massive increase in lipid biosynthesis required at this stage [48].

It is also worth highlighting that, while WT myelin at P20 is quite different in lipid composition compared to earlier time points (i.e., P5 and P10), CMT1A myelin at P20 is still very similar to early postnatal myelin (**Figure 1a**). This suggests that CMT1A myelin maturation is impaired, and the time frame in which myelin maturation occurs might be shifted in CMT1A rats. From the molecular standpoint, CMT1A myelin displays an imbalance between long- and short/medium-chain lipids. Given that the high proportion of saturated long-chain lipid species likely confers to myelin its specific biophysical properties [47], including ion permeability, fluidity, and localization and maintenance of ion channel clusters [76–78], we speculate that this could be a critical aspect underlying the altered functionality of CMT1A myelin.

Taking into account the difference in developmental stages between rats and humans, the time interval P10–P20 in rats corresponds approximately to an age of 1–2 years in humans [79,80]. Notably, CMT1A children under 1 year old have a neurological picture comparable to healthy subjects of equal age; structural and neurophysiological abnormalities appear by the age of 2 years in these young patients, corresponding to the temporal window P10–P20 in rats, when the delay in myelin maturation becomes appreciable. From a translational perspective, the consistency of our findings in rats with the progression of CMT1A in humans is quite remarkable.

Moreover, it is well known that the structural parameters of the fibers physiologically evolve during development, in order to allow an efficient propagation of electrical impulses along the nerves [73,81]. In particular, axonal diameter is directly correlated with conduction velocity and, by axon-glia interaction, guides the radial and longitudinal growth of myelin, impacting myelin thickness and internodal length [82–84]. In fact, as theoretically expected, among the different morphometric parameters analyzed, the most prominent defect we observed in CMT1A nerves was delayed and impaired axonal growth. Indeed, as we showed here, the lack of development of the largest MFs and the persistence of small fibers in adult nerves, lead to a homogeneous cluster of immature fibers, which are likely responsible for the electrophysiological properties of CMT1A peripheral nerves (i.e., low conduction velocity) [73].

Furthermore, axonal defects have also been described in other murine models of peripheral

neuropathies; for example, in mouse models of CMT1A, HNPP, and CMT4F, the depletion of large-caliber axons and the shortening of internodal length are hallmarks that become evident with age and are present in both peripheral nerves and spinal cord roots [19,71]. Given that these different neuropathies share some neuropathological features, one could also hypothesize a common aberrant mechanism involving pathological axon-glia interactions and causing an immature-like state of the fiber, bringing attention to the axon as a possible primary target for therapeutic approaches.

In CMT1A nerves, small-caliber fibers also appear hypermyelinated and are responsible for the decreased average G-Ratio [14,15]. Whether hypermyelination originates from an increased number of stacked myelin lamellae or altered compaction during myelination is still unknown. Certainly, this hypermyelination appears at a very early stage of development and persists throughout adult life.

To further support the immature phenotype of CMT1A nerves, we detected a prolonged presence of metabolically active SCs (hyperintense cells), that progressively decrease in number during development and almost completely disappear after the first month of life, suggesting an important role during development.

Our data also highlight a further evolution up to P180, indicating that PNS maturation is not complete after the myelination peak [39,85]. In this temporal window of six months, the rat completes skeletal muscle maturation and massively increases in body size and weight; realistically, the continuous evolution of PNS myelin lipid composition and structure that we observed parallels the physiological rat growth, as already described for the CNS [81,86]. This time interval is equivalent to adolescence/early adulthood in humans [80]. This observation is noteworthy because it offers a solid rationale for considering this extended temporal window for therapeutic intervention in CMT1A and other PNS myelin diseases.

The second part of this work is based on the hypothesis that gene therapy based on allele-specific silencing is an effective strategy to treat CMT1B patients with dominant-negative or gain-of-function *MPZ* mutations. We identified several sequences that strongly suppressed the mutant MPZ-D61N protein, with a minor effect on the WT. If the rescue experiment of $Mpz^{D61N/WT}$ DRG cultures will show a clear rescue of the dysmyelinating phenotype, we will also perform an in vivo rescue experiment on $Mpz^{D61N/WT}$ mice, by injecting them intrathecally with an AAV shRNA expression vector. We will then evaluate these mice for several outcome measures. The most important outcome we hope to obtain is the improvement of the motor performance of $Mpz^{D61N/WT}$ mice, since motor deficit is the most debilitating symptom in most CMT1B patients. However, we will also include secondary outcome measures, including histological parameters (such as myelinated area, myelin thickness, and G-Ratio) and molecular features (among which *Runx2*, *Apod*, *Pmp22*, and *Mbp* gene expression levels). It is also possible that improvements in these measures may not correspond to a significant improvement in motor performance. In this scenario, we would still consider the project a partial success, as it would support the validity of our approach for less severe forms of CMT1B.

Overall, we established a rigorous framework for optimization of allele-specific silencing strategies. However, it is still possible that the siRNA sequences selected *in vitro* will not be able to effectively silence the mutant MPZ-D61N allele *ex vivo* and *in vivo*. For example, the siRNA sequences may fail to bind the target mRNA region due to a particular secondary structure acquired by the *Mpz* mRNA or to the steric hindrance of mRNA-binding proteins that may bind a region in the proximity of the mutated nucleotide. Differences in the silencing performance of the siRNA sequences between the in vitro and *ex vivo*/*in vivo* models may be also due to the fact that, in the double fluorescence reporter assay, the

expression vectors for the mutant and the WT *Mpz* genes carried their cDNA sequence, leading to the production of an mRNA that did not undergo splicing. This may potentially result in an mRNA with different chemical and structural features compared to the one synthesized physiologically by SCs.

Hopefully, our results will provide the proof of principle that allele-specific RNA interference has potential therapeutic efficacy for CMT subtypes caused by gain-of-function and dominant-negative mutations.

Conclusions

In conclusion, this Ph.D. work provides novel mechanistic insights into the pathogenesis and therapeutic targeting of CMT1 neuropathies by addressing two major unmet needs in the field: understanding disease onset during development and tailoring mutation-specific therapeutic strategies. By integrating longitudinal lipidomic, morphometric, and ultrastructural analyses, we demonstrated that CMT1A is fundamentally a neurodevelopmental disorder characterized by a delayed and incomplete maturation of both axons and myelin. The identification of a critical developmental window in which myelin lipid composition and axonal growth fail to mature establishes a new conceptual framework for CMT1A etiopathology and provides a strong rationale for early therapeutic intervention.

In parallel, this work advances the field of CMT1B by exploiting a clinically relevant knock-in model to develop a rigorous proof-of-principle strategy for allele-specific gene silencing. Together, these complementary approaches move beyond descriptive pathology to define disease-driving mechanisms and actionable therapeutic paradigms, thereby contributing both fundamental knowledge and translational direction to the broader field of inherited peripheral neuropathies.

Bibliography

1. Ma, M.; Li, Y.; Dai, S.; Chu, M.; Sun, L.; Liu, L.; Zhou, J.-C. A Meta-Analysis on the Prevalence of Charcot–Marie–Tooth Disease and Related Inherited Peripheral Neuropathies. *J Neurol* **2023**, *270*, 2468–2482, doi:10.1007/s00415-023-11559-8.
2. Theadom, A.; Roxburgh, R.; MacAulay, E.; O'Grady, G.; Burns, J.; Parmar, P.; Jones, K.; Rodrigues, M. Prevalence of Charcot-Marie-Tooth Disease across the Lifespan: A Population-Based Epidemiological Study. *BMJ Open* **2019**, *9*, e029240, doi:10.1136/bmjopen-2019-029240.
3. Berciano, J.; García, A.; Gallardo, E.; Peeters, K.; Pelayo-Negro, A.L.; Álvarez-Paradelo, S.; Gazulla, J.; Martínez-Tames, M.; Infante, J.; Jordanova, A. Intermediate Charcot–Marie–Tooth Disease: An Electrophysiological Reappraisal and Systematic Review. *J Neurol* **2017**, *264*, 1655–1677, doi:10.1007/s00415-017-8474-3.
4. Saporta, A.S.D.; Sottile, S.L.; Miller, L.J.; Feely, S.M.E.; Siskind, C.E.; Shy, M.E. Charcot-Marie-Tooth Disease Subtypes and Genetic Testing Strategies. *Annals of Neurology* **2011**, *69*, 22–33, doi:10.1002/ana.22166.
5. Dong, H.; Qin, B.; Zhang, H.; Lei, L.; Wu, S. Current Treatment Methods for Charcot–Marie–Tooth Diseases. *Biomolecules* **2024**, *14*, 1138, doi:10.3390/biom14091138.
6. Timmerman, V.; Nelis, E.; Van Hul, W.; Nieuwenhuijsen, B.W.; Chen, K.L.; Wang, S.; Othman, K.B.; Cullen, B.; Leach, R.J.; Hanemann, C.O.; et al. The Peripheral Myelin Protein Gene PMP–22 Is Contained within the Charcot–Marie–Tooth Disease Type 1A Duplication. *Nat Genet* **1992**, *1*, 171–175, doi:10.1038/ng0692-171.
7. Roa, B.B.; Lupski, J.R. Molecular Basis of Charcot-Marie-Tooth Disease Type 1A: Gene Dosage as a Novel Mechanism for a Common Autosomal Dominant Condition. *The*

American Journal of the Medical Sciences **1993**, *306*, 177–184, doi:10.1097/00000441-199309000-00010.
8. Hertzog, N.; Jacob, C. Mechanisms and Treatment Strategies of Demyelinating and Dysmyelinating Charcot-Marie-Tooth Disease. *Neural Regen Res* **2023**, *18*, 1931–1939, doi:10.4103/1673-5374.367834.
9. Li, J. Caveats in the Established Understanding of CMT1A. *Ann Clin Transl Neurol* **2017**, *4*, 601–607, doi:10.1002/acn3.432.
10. Nobbio, L.; Visigalli, D.; Radice, D.; Fiorina, E.; Solari, A.; Lauria, G.; Reilly, M.M.; Santoro, L.; Schenone, A.; Pareyson, D.; et al. PMP22 Messenger RNA Levels in Skin Biopsies: Testing the Effectiveness of a Charcot-Marie-Tooth 1A Biomarker. *Brain* **2014**, *137*, 1614–1620, doi:10.1093/brain/awu071.
11. Lewis, R.A.; Sumner, A.J.; Brown, M.J.; Asbury, A.K. Multifocal Demyelinating Neuropathy with Persistent Conduction Block. *Neurology* **1982**, *32*, 958–958, doi:10.1212/WNL.32.9.958.
12. Manganelli, F.; Pisciotta, C.; Reilly, M.M.; Tozza, S.; Schenone, A.; Fabrizi, G.M.; Cavallaro, T.; Vita, G.; Padua, L.; Gemignani, F.; et al. Nerve Conduction Velocity in CMT 1A: What Else Can We Tell? *Euro J of Neurology* **2016**, *23*, 1566–1571, doi:10.1111/ene.13079.
13. García, A.; Combarros, O.; Calleja, J.; Berciano, J. Charcot-Marie-Tooth Disease Type 1A with 17p Duplication in Infancy and Early Childhood: A Longitudinal Clinical and Electrophysiologic Study. *Neurology* **1998**, *50*, 1061–1067, doi:10.1212/WNL.50.4.1061.
14. Gabreëls-Festen, A.A.W.M.; Bolhuis, P.A.; Hoogendijk, J.E.; Valentijn, L.J.; Eshuis, E.J.H.M.; Gabre□ls, F.J.M. Charcot-Marie-Tooth Disease Type 1A: Morphological Phenotype of the 17p Duplication versus PMP22 Point Mutations. *Acta Neuropathol* **1995**, *90*, 645–649, doi:10.1007/BF00318579.
15. Gabreëls-Festen, A.; Wetering, R.V. Human Nerve Pathology Caused by Different Mutational Mechanisms of the PMP22 Gene. *Annals of the New York Academy of Sciences* **1999**, *883*, 336–343.
16. Fledrich, R.; Kungl, T.; Nave, K.-A.; Stassart, R.M. Axo-Glial Interdependence in Peripheral Nerve Development. *Development* **2019**, *146*, dev151704, doi:10.1242/dev.151704.
17. Oka, N.; Kawasaki, T.; Unuma, T.; Shigematsu, K.; Sugiyama, H. Different Profiles of Onion Bulb in CIDP and CMT1A in Relation to Extracellular Matrix. *Clin Neuropathol* **2013**, *32*, 406–412, doi:10.5414/NP300597.
18. Li, J. Molecular Regulators of Nerve Conduction — Lessons from Inherited Neuropathies and Rodent Genetic Models. *Experimental Neurology* **2015**, *267*, 209–218, doi:10.1016/j.expneurol.2015.03.009.
19. Sancho, S.; Magyar, J.P.; Aguzzi, A.; Suter1, U. Distal Axonopathy in Peripheral Nerves of PMP22-Mutant Mice. *Brain* **1999**, *122*, 1563–1577, doi:10.1093/brain/122.8.1563.
20. Eichel, M.A.; Gargareta, V.-I.; D'Este, E.; Fledrich, R.; Kungl, T.; Buscham, T.J.; Lüders, K.A.; Miracle, C.; Jung, R.B.; Distler, U.; et al. CMTM6 Expressed on the Adaxonal Schwann Cell Surface Restricts Axonal Diameters in Peripheral Nerves. *Nat Commun* **2020**, *11*, 4514, doi:10.1038/s41467-020-18172-7.
21. Hoffman, P.N.; Griffin, J.W.; Price, D.L. Control of Axonal Caliber by Neurofilament Transport. *The Journal of cell biology* **1984**, *99*, 705–714, doi:10.1083/jcb.99.2.705.
22. Fledrich, R.; Stassart, R.M.; Klink, A.; Rasch, L.M.; Prukop, T.; Haag, L.; Czesnik, D.; Kungl, T.; Abdelaal, T.A.M.; Keric, N.; et al. Soluble Neuregulin-1 Modulates Disease Pathogenesis in Rodent Models of Charcot-Marie-Tooth Disease 1A. *Nature medicine* **2014**, *20*, 1055–1061, doi:10.1038/nm.3664.

23. Hattori, N.; Yamamoto, M.; Yoshihara, T.; Koike, H.; Nakagawa, M.; Yoshikawa, H.; Ohnishi, A.; Hayasaka, K.; Onodera, O.; Baba, M.; et al. Demyelinating and Axonal Features of Charcot-Marie-Tooth Disease with Mutations of Myelin-Related Proteins (PMP22, MPZ and Cx32): A Clinicopathological Study of 205 Japanese Patients. *Brain* **2003**, *126*, 134–151, doi:10.1093/brain/awg012.
24. Sander, S.; Nicholson, G.A.; Ouvrier, R.A.; McLeod, J.G.; Pollard, J.D. Charcot-Marie-Tooth Disease: Histopathological Features of the Peripheral Myelin Protein (PMP22) Duplication (CMT1A) and Connexin32 Mutations (CMTX1). *Muscle Nerve* **1998**, *21*, 217–225, doi:10.1002/(SICI)1097-4598(199802)21:2%3C217::AID-MUS9%3E3.0.CO;2-E.
25. Fledrich, R.; Abdelaal, T.; Rasch, L.; Bansal, V.; Schütza, V.; Brügger, B.; Lüchtenborg, C.; Prukop, T.; Stenzel, J.; Rahman, R.U.; et al. Targeting Myelin Lipid Metabolism as a Potential Therapeutic Strategy in a Model of CMT1A Neuropathy. *Nat Commun* **2018**, *9*, 3025, doi:10.1038/s41467-018-05420-0.
26. Visigalli, D.; Capodivento, G.; Basit, A.; Fernández, R.; Hamid, Z.; Pencová, B.; Gemelli, C.; Marubbi, D.; Pastorino, C.; Luoma, A.M.; et al. Exploiting Sphingo- and Glycerophospholipid Impairment to Select Effective Drugs and Biomarkers for CMT1A. *Front. Neurol.* **2020**, *11*, 903, doi:10.3389/fneur.2020.00903.
27. Giese, K.P.; Martini, R.; Lemke, G.; Soriano, P.; Schachner, M. Mouse P0 Gene Disruption Leads to Hypomyelination, Abnormal Expression of Recognition Molecules, and Degeneration of Myelin and Axons. *Cell* **1992**, *71*, 565–576, doi:10.1016/0092-8674(92)90591-y.
28. Zielasek, J.; Martini, R.; Toyka, K.V. Functional Abnormalities in P0-Deficient Mice Resemble Human Hereditary Neuropathies Linked to P0 Gene Mutations. *Muscle & Nerve* **1996**, *19*, 946–952, doi:10.1002/(SICI)1097-4598(199608)19:8%3C946::AID-MUS2%3E3.0.CO;2-8.
29. Fridman, V.; Bundy, B.; Reilly, M.M.; Pareyson, D.; Bacon, C.; Burns, J.; Day, J.; Feely, S.; Finkel, R.S.; Grider, T.; et al. CMT Subtypes and Disease Burden in Patients Enrolled in the Inherited Neuropathies Consortium Natural History Study: A Cross-Sectional Analysis. *J Neurol Neurosurg Psychiatry* **2015**, *86*, 873–878, doi:10.1136/jnnp-2014-308826.
30. Mandich, P.; Fossa, P.; Capponi, S.; Geroldi, A.; Acquaviva, M.; Gulli, R.; Ciotti, P.; Manganelli, F.; Grandis, M.; Bellone, E. Clinical Features and Molecular Modelling of Novel MPZ Mutations in Demyelinating and Axonal Neuropathies. *Eur J Hum Genet* **2009**, *17*, 1129–1134, doi:10.1038/ejhg.2009.37.
31. Shy, M.E.; Jáni, A.; Krajewski, K.; Grandis, M.; Lewis, R.A.; Li, J.; Shy, R.R.; Balsamo, J.; Lilien, J.; Garbern, J.Y.; et al. Phenotypic Clustering in MPZ Mutations. *Brain* **2004**, *127*, 371–384, doi:10.1093/brain/awh048.
32. Prada, V.; Passalacqua, M.; Bono, M.; Luzzi, P.; Scazzola, S.; Nobbio, L.A.; Capponi, S.; Bellone, E.; Mandich, P.; Mancardi, G.; et al. Gain of Glycosylation: A New Pathomechanism of Myelin Protein Zero Mutations. *Annals of Neurology* **2012**, *71*, 427–431, doi:10.1002/ana.22695.
33. Yonekawa, T.; Komaki, H.; Saito, Y.; Takashima, H.; Sasaki, M. Congenital Hypomyelinating Neuropathy Attributable to a De Novo p.Asp61Asn Mutation of the Myelin Protein Zero Gene. *Pediatric Neurology* **2013**, *48*, 59–62, doi:10.1016/j.pediatrneurol.2012.09.011.
34. Veneri, F.A.; Prada, V.; Mastrangelo, R.; Ferri, C.; Nobbio, L.; Passalacqua, M.; Milanesi, M.; Bianchi, F.; Del Carro, U.; Vallat, J.-M.; et al. A Novel Mouse Model of CMT1B Identifies Hyperglycosylation as a New Pathogenetic Mechanism. *Human Molecular Genetics* **2022**, *31*, 4255–4274, doi:10.1093/hmg/ddac170.

35. Pisciotta, C.; Saveri, P.; Pareyson, D. Challenges in Treating Charcot-Marie-Tooth Disease and Related Neuropathies: Current Management and Future Perspectives. *Brain Sciences* **2021**, *11*, 1447, doi:10.3390/brainsci11111447.
36. Stavrou, M.; Kleopa, K.A. Gene Therapies for CMT Neuropathies: From the Bench to the Clinic. *Current Opinion in Neurology* **2024**, *37*, 445, doi:10.1097/WCO.0000000000001289.
37. Wrabetz, L.; Feltri, M.L.; Quattrini, A.; Imperiale, D.; Previtali, S.; D'Antonio, M.; Martini, R.; Yin, X.; Trapp, B.D.; Zhou, L.; et al. P0 Glycoprotein Overexpression Causes Congenital Hypomyelination of Peripheral Nerves. *Journal of Cell Biology* **2000**, *148*, 1021–1034, doi:10.1083/jcb.148.5.1021.
38. Howard, P.; Feely, S.M.E.; Grider, T.; Bacha, A.; Scarlato, M.; Fazio, R.; Quattrini, A.; Shy, M.E.; Previtali, S.C. Loss of Function MPZ Mutation Causes Milder CMT1B Neuropathy. *Journal of the Peripheral Nervous System* **2021**, *26*, 177–183, doi:10.1111/jns.12452.
39. Sereda, M.; Griffiths, I.; Pühlhofer, A.; Stewart, H.; Rossner, M.J.; Zimmermann, F.; Magyar, J.P.; Schneider, A.; Hund, E.; Meinck, H.-M.; et al. A Transgenic Rat Model of Charcot-Marie-Tooth Disease. *Neuron* **1996**, *16*, 1049–1060, doi:10.1016/S0896-6273(00)80128-2.
40. Capodivento, G.; Visigalli, D.; Garnero, M.; Fancellu, R.; Ferrara, M.D.; Basit, A.; Hamid, Z.; Pastore, V.P.; Garibaldi, S.; Armirotti, A.; et al. Sphingomyelin as a Myelin Biomarker in CSF of Acquired Demyelinating Neuropathies. *Sci Rep* **2017**, *7*, 7831, doi:10.1038/s41598-017-08314-1.
41. Larocca, J.N.; Norton, W.T. Isolation of Myelin. *CP Cell Biology* **2006**, *33*, doi:10.1002/0471143030.cb0325s33.
42. Dull, T.; Zufferey, R.; Kelly, M.; Mandel, R.J.; Nguyen, M.; Trono, D.; Naldini, L. A Third-Generation Lentivirus Vector with a Conditional Packaging System. *J. Virol.* **1998**, *72*, 8463–8471, doi:10.1128/JVI.72.11.8463-8471.1998.
43. Schindelin, J.; Arganda-Carreras, I.; Frise, E.; Kaynig, V.; Longair, M.; Pietzsch, T.; Preibisch, S.; Rueden, C.; Saalfeld, S.; Schmid, B.; et al. Fiji: An Open-Source Platform for Biological-Image Analysis. *Nat Methods* **2012**, *9*, 676–682, doi:10.1038/nmeth.2019.
44. Moruzzo, D.; Nobbio, L.; Sterlini, B.; Consalez, G.G.; Benfenati, F.; Schenone, A.; Corradi, A. The Transcription Factors EBF1 and EBF2 Are Positive Regulators of Myelination in Schwann Cells. *Mol Neurobiol* **2017**, *54*, 8117–8127, doi:10.1007/s12035-016-0296-2.
45. Molenaar, M.R.; Jeucken, A.; Wassenaar, T.A.; Van De Lest, C.H.A.; Brouwers, J.F.; Helms, J.B. LION/Web: A Web-Based Ontology Enrichment Tool for Lipidomic Data Analysis. *GigaScience* **2019**, *8*, giz061, doi:10.1093/gigascience/giz061.
46. Molenaar, M.R.; Haaker, M.W.; Vaandrager, A.B.; Houweling, M.; Helms, J.B. Lipidomic Profiling of Rat Hepatic Stellate Cells during Activation Reveals a Two-Stage Process Accompanied by Increased Levels of Lysosomal Lipids. *Journal of Biological Chemistry* **2023**, *299*, 103042, doi:10.1016/j.jbc.2023.103042.
47. Chrast, R.; Saher, G.; Nave, K.-A.; Verheijen, M.H.G. Lipid Metabolism in Myelinating Glial Cells: Lessons from Human Inherited Disorders and Mouse Models. *J Lipid Res* **2011**, *52*, 419–434, doi:10.1194/jlr.R009761.
48. Poitelon, Y.; Kopec, A.M.; Belin, S. Myelin Fat Facts: An Overview of Lipids and Fatty Acid Metabolism. *Cells* **2020**, *9*, 812, doi:10.3390/cells9040812.
49. Montani, L. Lipids in Regulating Oligodendrocyte Structure and Function. *Seminars in Cell & Developmental Biology* **2021**, *112*, 114–122, doi:10.1016/j.semcdb.2020.07.016.

50. Harayama, T.; Riezman, H. Understanding the Diversity of Membrane Lipid Composition. *Nat Rev Mol Cell Biol* **2018**, *19*, 281–296, doi:10.1038/nrm.2017.138.
51. Schwarz, D.S.; Blower, M.D. The Endoplasmic Reticulum: Structure, Function and Response to Cellular Signaling. *Cell. Mol. Life Sci.* **2016**, *73*, 79–94, doi:10.1007/s00018-015-2052-6.
52. Federovitch, C.M.; Ron, D.; Hampton, R.Y. The Dynamic ER: Experimental Approaches and Current Questions. *Current Opinion in Cell Biology* **2005**, *17*, 409–414, doi:10.1016/j.ceb.2005.06.010.
53. Stavrou, M.; Kagiava, A.; Choudury, S.G.; Jennings, M.J.; Wallace, L.M.; Fowler, A.M.; Heslegrave, A.; Richter, J.; Tryfonos, C.; Christodoulou, C.; et al. A Translatable RNAi-Driven Gene Therapy Silences *PMP22/Pmp22* Genes and Improves Neuropathy in CMT1A Mice. *J Clin Invest* **2022**, *132*, doi:10.1172/JCI159814.
54. Boutary, S.; Caillaud, M.; El Madani, M.; Vallat, J.-M.; Loisel-Duwattez, J.; Rouyer, A.; Richard, L.; Gracia, C.; Urbinati, G.; Desmaële, D.; et al. Squalenoyl siRNA PMP22 Nanoparticles Are Effective in Treating Mouse Models of Charcot-Marie-Tooth Disease Type 1 A. *Commun Biol* **2021**, *4*, 1–14, doi:10.1038/s42003-021-01839-2.
55. Lee, J.-S.; Chang, E.H.; Koo, O.J.; Jwa, D.H.; Mo, W.M.; Kwak, G.; Moon, H.W.; Park, H.T.; Hong, Y.B.; Choi, B.-O. *Pmp22* Mutant Allele-Specific siRNA Alleviates Demyelinating Neuropathic Phenotype *in Vivo*. *Neurobiology of Disease* **2017**, *100*, 99–107, doi:10.1016/j.nbd.2017.01.006.
56. Pereira, J.A.; Lebrun-Julien, F.; Suter, U. Molecular Mechanisms Regulating Myelination in the Peripheral Nervous System. *Trends in Neurosciences* **2012**, *35*, 123–134, doi:10.1016/j.tins.2011.11.006.
57. Snaidero, N.; Möbius, W.; Czopka, T.; Hekking, L.H.P.; Mathisen, C.; Verkleij, D.; Goebbels, S.; Edgar, J.; Merkler, D.; Lyons, D.A.; et al. Myelin Membrane Wrapping of CNS Axons by PI(3,4,5)P3-Dependent Polarized Growth at the Inner Tongue. *Cell* **2014**, *156*, 277–290, doi:10.1016/j.cell.2013.11.044.
58. Djannatian, M.; Radha, S.; Weikert, U.; Safaiyan, S.; Wrede, C.; Deichsel, C.; Kislinger, G.; Rhomberg, A.; Ruhwedel, T.; Campbell, D.S.; et al. Myelination Generates Aberrant Ultrastructure That Is Resolved by Microglia. *J Cell Biol* **2023**, *222*, e202204010, doi:10.1083/jcb.202204010.
59. Lori, S.; Bertini, G.; Bastianelli, M.; Gabbanini, S.; Gualandi, D.; Molesti, E.; Dani, C. Peripheral Nervous System Maturation in Preterm Infants: Longitudinal Motor and Sensory Nerve Conduction Studies. *Childs Nerv Syst* **2018**, *34*, 1145–1152, doi:10.1007/s00381-018-3778-x.
60. Farrar, M.A.; Park, S.B.; Lin, C.S.-Y.; Kiernan, M.C. Evolution of Peripheral Nerve Function in Humans: Novel Insights from Motor Nerve Excitability. *J Physiol* **2013**, *591*, 273–286, doi:10.1113/jphysiol.2012.240820.
61. Gamstorp, I. NORMAL CONDUCTION VELOCITY OF ULNAR, MEDIAN AND PERONEAL NERVES IN INFANCY, CHILDHOOD AND ADOLESCENCE. *Acta Paediatr Suppl (Upps)* **1963**, SUPPL146:68-76, doi:10.1111/j.1651-2227.1963.tb05519.x.
62. Jacobs, J.M.; Love, S. Qualitative and Quantitative Morphology of Human Sural Nerve at Different Ages. *Brain : a journal of neurology* **1985**, *108 (Pt 4)*, 897–924, doi:10.1093/brain/108.4.897.
63. Ouvrier, R.A.; Mcleod, J.G.; Conchin, T.E. THE HYPERTROPHIC FORMS OF HEREDITARY MOTOR AND SENSORY NEUROPATHY: A STUDY OF HYPERTROPHIC CHARCOT-MARIE-TOOTH DISEASE (HMSN TYPE I) AND DEJERINE-SOTTAS DISEASE (HMSN TYPE III) IN CHILDHOOD. *Brain* **1987**, *110*, 121–148, doi:10.1093/brain/110.1.121.

64. Davion, J.-B.; Cassim, F.; Péréon, Y.; Nguyen The Tich, S. Young Infants with PMP22 Duplication Can Have Minor Nerve Conduction Study Abnormalities. *Neurophysiologie Clinique* **2022**, *52*, 482–485, doi:10.1016/j.neucli.2022.09.007.
65. Patzig, J.; Jahn, O.; Tenzer, S.; Wichert, S.P.; De Monasterio-Schrader, P.; Rosfa, S.; Kuharev, J.; Yan, K.; Bormuth, I.; Bremer, J.; et al. Quantitative and Integrative Proteome Analysis of Peripheral Nerve Myelin Identifies Novel Myelin Proteins and Candidate Neuropathy Loci. *J. Neurosci.* **2011**, *31*, 16369–16386, doi:10.1523/JNEUROSCI.4016-11.2011.
66. Davis, D.L.; Mahawar, U.; Pope, V.S.; Allegood, J.; Sato-Bigbee, C.; Wattenberg, B.W. Dynamics of Sphingolipids and the Serine Palmitoyltransferase Complex in Rat Oligodendrocytes during Myelination. *Journal of Lipid Research* **2020**, *61*, 505–522, doi:10.1194/jlr.RA120000627.
67. Djuanda, D.; He, B.; Liu, X.; Xu, S.; Zhang, Y.; Xu, Y.; Zhu, Z. Comprehensive Analysis of Age-Related Changes in Lipid Metabolism and Myelin Sheath Formation in Sciatic Nerves. *J Mol Neurosci* **2021**, *71*, 2310–2323, doi:10.1007/s12031-020-01768-5.
68. Helbing, D.L.; Kirkpatrick, J.M.; Reuter, M.; Bischoff, J.; Stockdale, A.; Carlstedt, A.; Cirri, E.; Bauer, R.; Morrison, H. Proteomic Analysis of Peripheral Nerve Myelin during Murine Aging. *Front Cell Neurosci* **2023**, *17*, 1214003, doi:10.3389/fncel.2023.1214003.
69. Verheijen, M.H.G.; Camargo, N.; Verdier, V.; Nadra, K.; de Preux Charles, A.-S.; Médard, J.-J.; Luoma, A.; Crowther, M.; Inouye, H.; Shimano, H.; et al. SCAP Is Required for Timely and Proper Myelin Membrane Synthesis. *Proc Natl Acad Sci U S A* **2009**, *106*, 21383–21388, doi:10.1073/pnas.0905633106.
70. Siems, S.B.; Jahn, O.; Eichel, M.A.; Kannaiyan, N.; Wu, L.M.N.; Sherman, D.L.; Kusch, K.; Hesse, D.; Jung, R.B.; Fledrich, R.; et al. Proteome Profile of Peripheral Myelin in Healthy Mice and in a Neuropathy Model. *Elife* **2020**, *9*, e51406, doi:10.7554/eLife.51406.
71. Ziskind-Conhaim, L. Physiological and Morphological Changes in Developing Peripheral Nerves of Rat Embryos. *Developmental Brain Research* **1988**, *42*, 15–28, doi:10.1016/0165-3806(88)90198-8.
72. Vabnick, I.; Shrager, P. Ion Channel Redistribution and Function during Development of the Myelinated Axon. *J. Neurobiol.* **1998**, *37*, 80–96, doi:10.1002/(SICI)1097-4695(199810)37:1%3C80::AID-NEU7%3E3.0.CO;2-4.
73. Castelfranco, A.M.; Hartline, D.K. Evolution of Rapid Nerve Conduction. *Brain Research* **2016**, *1641*, 11–33, doi:10.1016/j.brainres.2016.02.015.
74. Olsen, A.S.B.; Færgeman, N.J. Sphingolipids: Membrane Microdomains in Brain Development, Function and Neurological Diseases. *Open Biol.* **2017**, *7*, 170069, doi:10.1098/rsob.170069.
75. Svennerholm, L.; Vanier, M.-T. The Distribution of Lipids in the Human Nervous System. IV. Fatty Acid Composition of Major Sphingolipids of Human Infant Brain. *Brain Research* **1973**, *55*, 413–423, doi:10.1016/0006-8993(73)90306-5.
76. Ishibashi, T.; Dupree, J.L.; Ikenaka, K.; Hirahara, Y.; Honke, K.; Peles, E.; Popko, B.; Suzuki, K.; Nishino, H.; Baba, H. A Myelin Galactolipid, Sulfatide, Is Essential for Maintenance of Ion Channels on Myelinated Axon But Not Essential for Initial Cluster Formation. *The Journal of Neuroscience* **2002**, *22*, 6507–6514, doi:10.1523/JNEUROSCI.22-15-06507.2002.
77. Simons, K.; Vaz, W.L.C. Model Systems, Lipid Rafts, and Cell Membranes. *Annu. Rev. Biophys. Biomol. Struct.* **2004**, *33*, 269–295, doi:10.1146/annurev.biophys.32.110601.141803.

78. Kakorin, S.; Brinkmann, U.; Neumann, E. Cholesterol Reduces Membrane Electroporation and Electric Deformation of Small Bilayer Vesicles. *Biophys Chem* **2005**, *117*, 155–171, doi:10.1016/j.bpc.2005.05.001.
79. Quinn, R. Comparing Rat's to Human's Age: How Old Is My Rat in People Years? *Nutrition* **2005**, *21*, 775–777, doi:10.1016/j.nut.2005.04.002.
80. Ghasemi, A.; Jeddi, S.; Kashfi, K. The Laboratory Rat: Age and Body Weight Matter. *EXCLI J* **2021**, *20*, 1431–1445, doi:10.17179/excli2021-4072.
81. Bandeira, F.; Lent, R.; Herculano-Houzel, S. Changing Numbers of Neuronal and Non-Neuronal Cells Underlie Postnatal Brain Growth in the Rat. *Proc. Natl. Acad. Sci. U.S.A.* **2009**, *106*, 14108–14113, doi:10.1073/pnas.0804650106.
82. Poitelon, Y.; Bogni, S.; Matafora, V.; Della-Flora Nunes, G.; Hurley, E.; Ghidinelli, M.; Katzenellenbogen, B.S.; Taveggia, C.; Silvestri, N.; Bachi, A.; et al. Spatial Mapping of Juxtacrine Axo-Glial Interactions Identifies Novel Molecules in Peripheral Myelination. *Nat Commun* **2015**, *6*, 8303, doi:10.1038/ncomms9303.
83. Taveggia, C.; Zanazzi, G.; Petrylak, A.; Yano, H.; Rosenbluth, J.; Einheber, S.; Xu, X.; Esper, R.M.; Loeb, J.A.; Shrager, P.; et al. Neuregulin-1 Type III Determines the Ensheathment Fate of Axons. *Neuron* **2005**, *47*, 681–694, doi:10.1016/j.neuron.2005.08.017.
84. Stassart, R.M.; Woodhoo, A. Axo-glial Interaction in the Injured PNS. *Developmental Neurobiology* **2021**, *81*, 490–506, doi:10.1002/dneu.22771.
85. Agrawal, D.; Hawk, R.; Avila, R.L.; Inouye, H.; Kirschner, D.A. Internodal Myelination during Development Quantitated Using X-Ray Diffraction. *Journal of structural biology* **2009**, *168*, 521–526, doi:10.1016/j.jsb.2009.06.019.
86. Fu, Y.; Yuan, Y.; Halliday, G.; Rusznák, Z.; Watson, C.; Paxinos, G. A Cytoarchitectonic and Chemoarchitectonic Analysis of the Dopamine Cell Groups in the Substantia Nigra, Ventral Tegmental Area, and Retrorubral Field in the Mouse. *Brain Structure and Function* **2012**, *217*, 591–612, doi:10.1007/s00429-011-0349-2.

Supplementary Figures

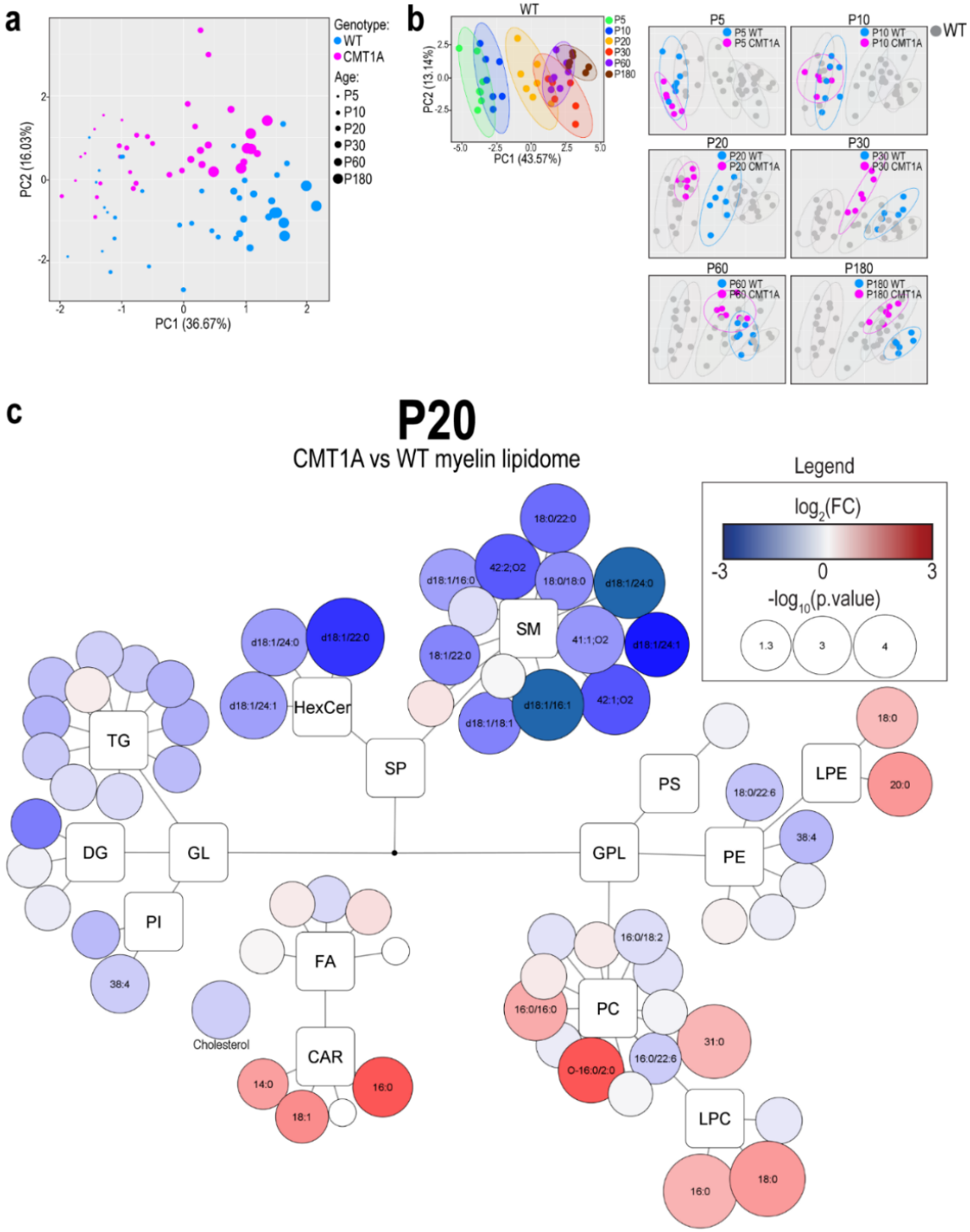

Supplementary Figure.1 Lipidomic data. (**a**) PCA plot of lipidomic data from WT and CMT1A purified peripheral myelin extracted from the sciatic nerve of P5, P10, P20, P30, P60, and P180 rats. n = at least 6 samples for each group. (**b**) PCA plots showing CMT1A samples from each time point together with WT samples, to highlight the maturation delay experienced by CMT1A myelin. (**c**) Simplified network visualization of lipid metabolism showing alterations in myelin lipid profile of P20 CMT1A rats, as compared to WT. Each dot represents a lipid species, dot size expresses the significance according to p value, while the color intensity defines the degree of up (red) and downregulation (blue) according to the fold change (as CMT1A vs WT). The lipids showing a statistically significant difference are annotated. n = 7 WT and 7 CMT1A samples; for each sample, sciatic nerves from 5 different animals were pulled together to obtain enough material for the analysis. p values were calculated using a two-tailed unpaired Student's t-test.

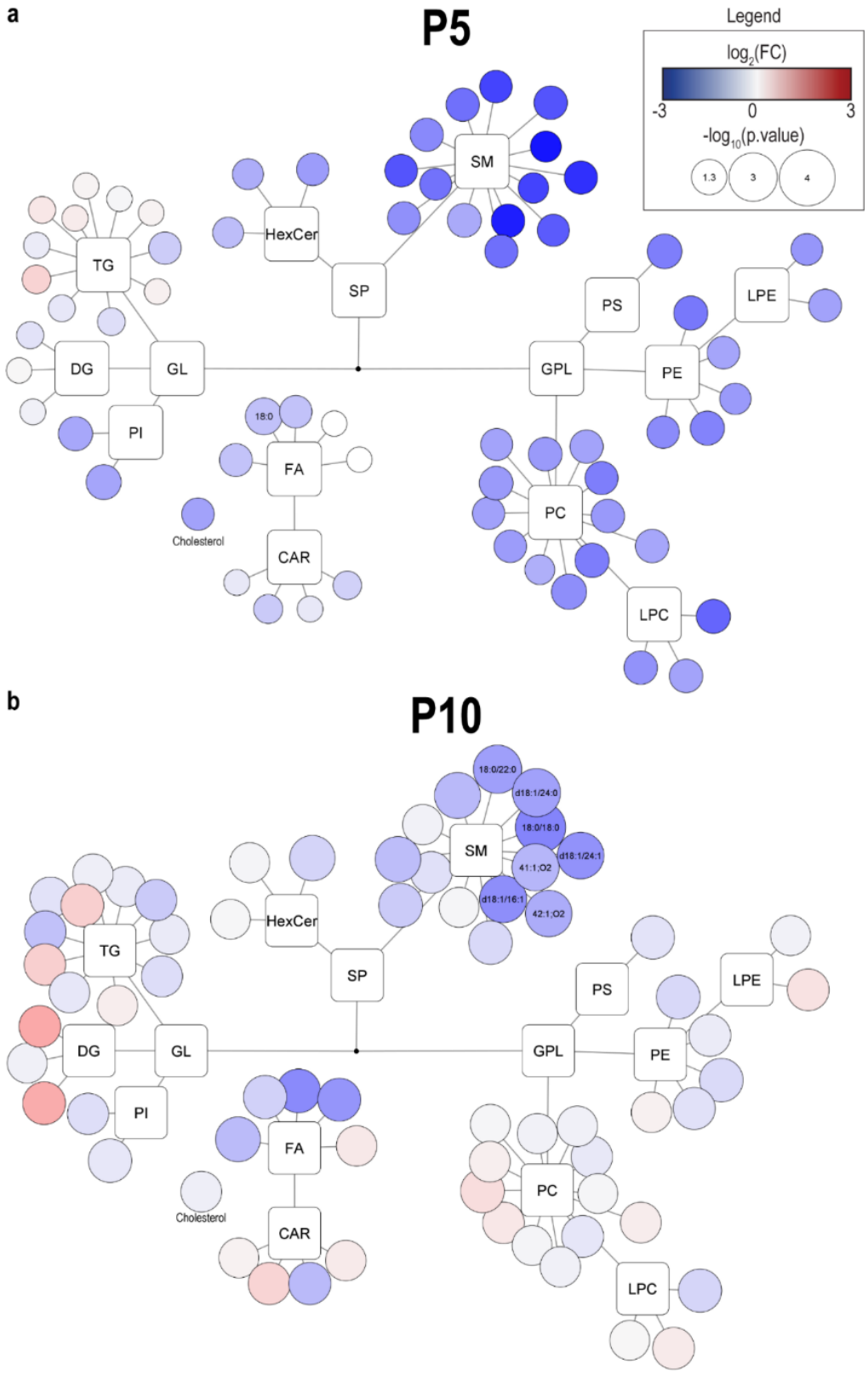

Supplementary Figure 2. Lipidomic data at P5 and P10. (**a-b**) Simplified network visualization of lipid metabolism showing alterations in myelin lipid profile of P5 (**a**) and P10 (**b**) CMT1A rats, as compared to WT. Each dot represents a lipid species, dot size expresses the significance according to p value, while the color intensity defines the degree of up (red) and downregulation (blue) according to the fold change (as CMT1A vs WT). The lipids showing a statistically significant difference are annotated. n = 7 WT and 7 CMT1A samples; for each sample, sciatic nerves from 5 different animals were pulled together to obtain enough material for the analysis. p values were calculated using a two-tailed unpaired Student's t-test.

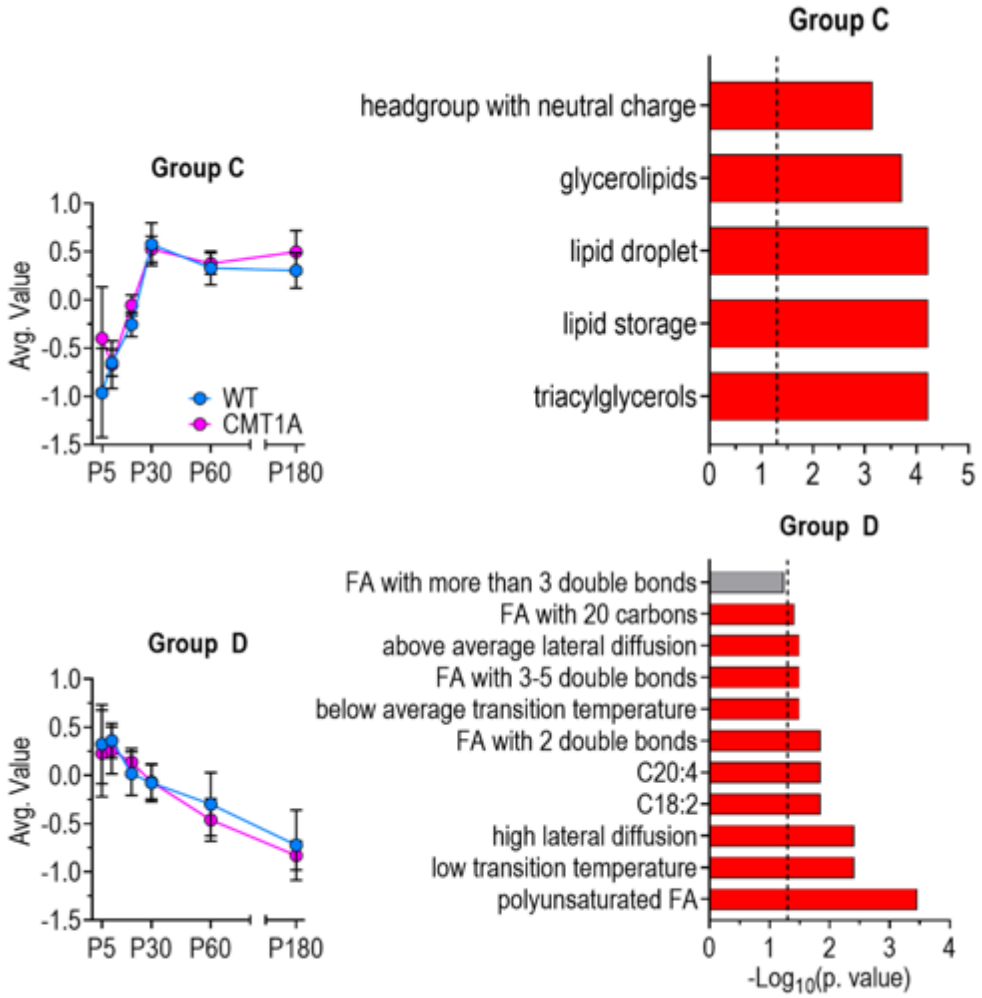

Supplementary Figure 3. Lipidomic data and lipid enrichment analysis. (**a**) On the left, average value of lipids in group C (top) and D (bottom); on the right, results of enrichment analysis performed using LION software on lipids in group C (top) and D (bottom). The dotted line marks the p value significance threshold (0.05).

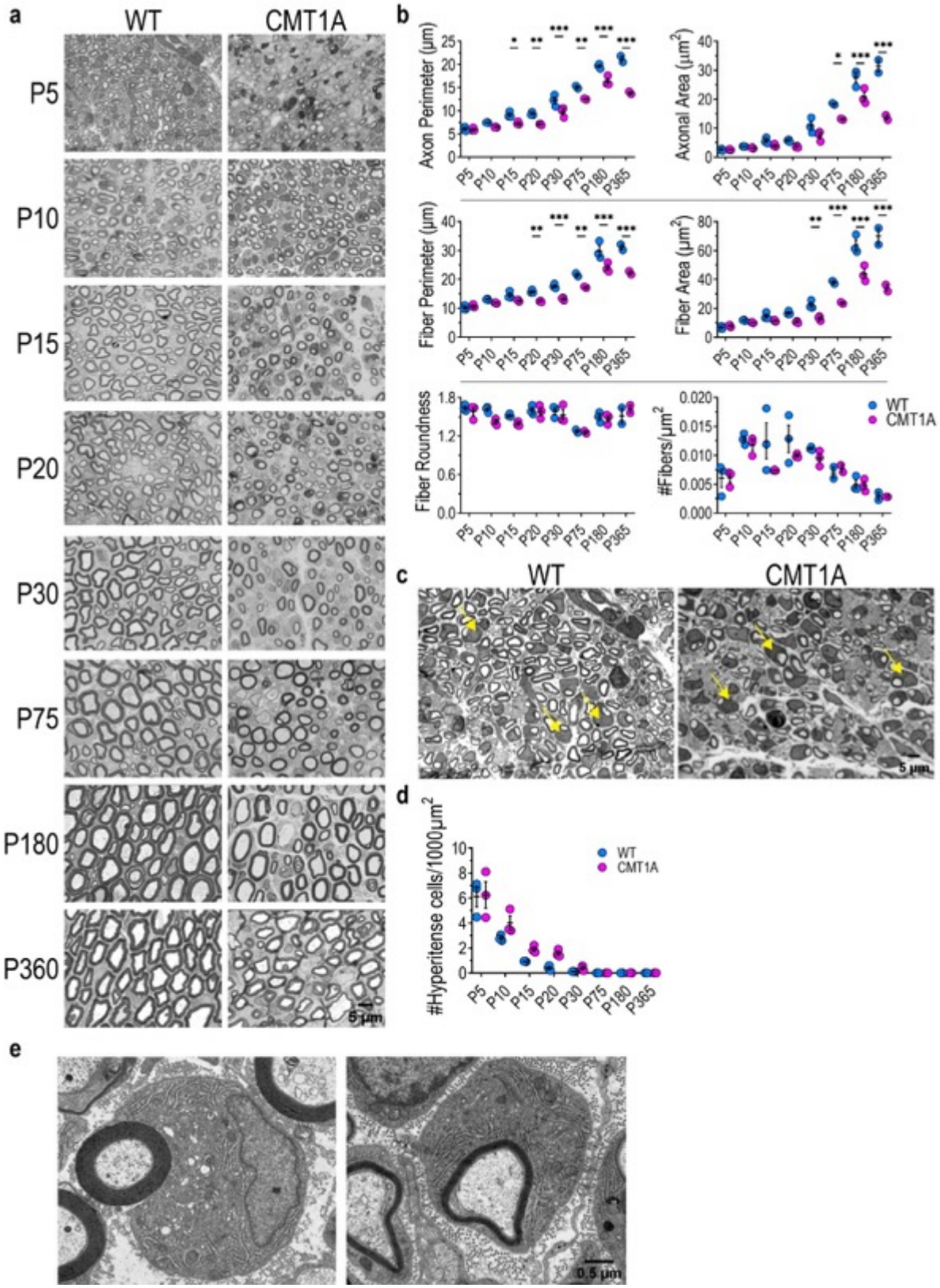

Supplementary Figure 4. Morphometric parameters and hyperintense cells. (**a**) Micrographs of cross-sections of WT and CMT1A sciatic nerves at all time points analyzed in this study, stained with toluidine blue. (**b**) Morphometric parameters measured from WT and CMT1A sciatic nerve sections. (**c**) Micrographs of cross-sections of P5 WT and CMT1A sciatic nerves stained with toluidine blue; yellow arrows indicate hyperintense cells. (**d**) Hyperintense cell density in WT and CMT1A sciatic nerves at different time points. n = 3 rats for each genotype and each time point. At P5, at least 800 myelinated fibers were evaluated for each rat; at later time points, at least 3000 fibers were evaluated for each rat. (**e**) Transmission electron microscopy micrographs of

representative hyperintense cells. Scale bar: 0.5 µm. Values are presented as mean ± SEM. * $p < 0.05$, ** $p < 0.01$, *** $p < 0.001$. p values were calculated using Kruskal-Wallis test followed by Sidak's multiple comparisons test between the two genotypes for each time point.

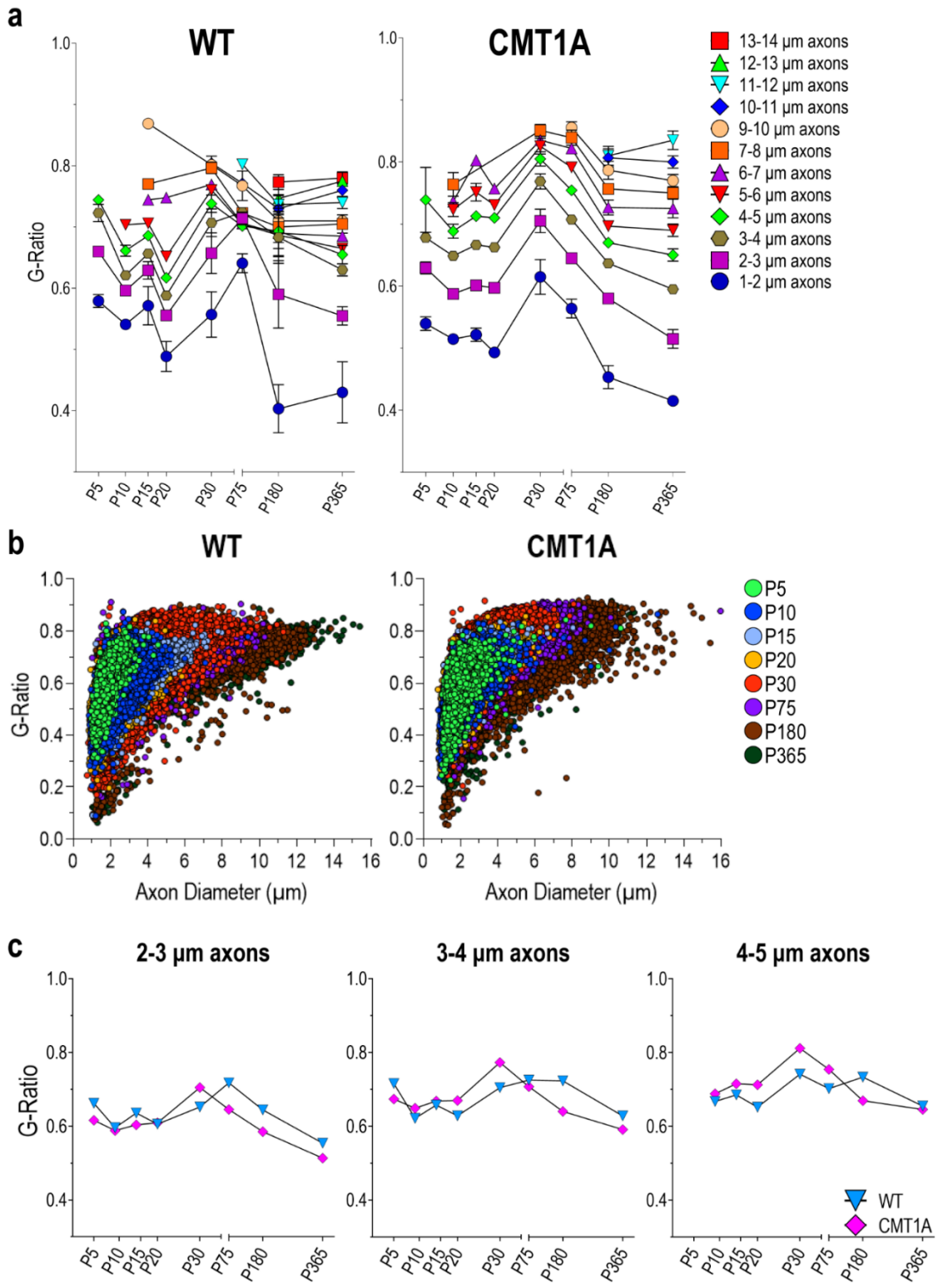

Supplementary Figure 5. Analysis of G-Ratio evolution during development (**a**) Developmental trajectories of G-Ratio in WT (left) and CMT1A (right) rat sciatic nerves from early postnatal days to adulthood, measured for each axonal class. Fibers were classified based on axon diameter. (**b**) Scatterplots showing the G-Ratio plotted against the axon diameter of WT and CMT1A sciatic nerve fibers at different time points. (**c**) Same data as in **a**,

but WT and CMT1A data of the same axonal class are plotted together. Values are presented as mean ± SEM; for some values, error bars are not visible because they are covered by the symbol. *** $p < 0.001$. n = 3000 myelinated fibers from 3 different animals per genotype were evaluated at P5, 9000 myelinated fibers from 3 different animals per genotype were evaluated at later time points. p values were calculated as in Figure 3c.

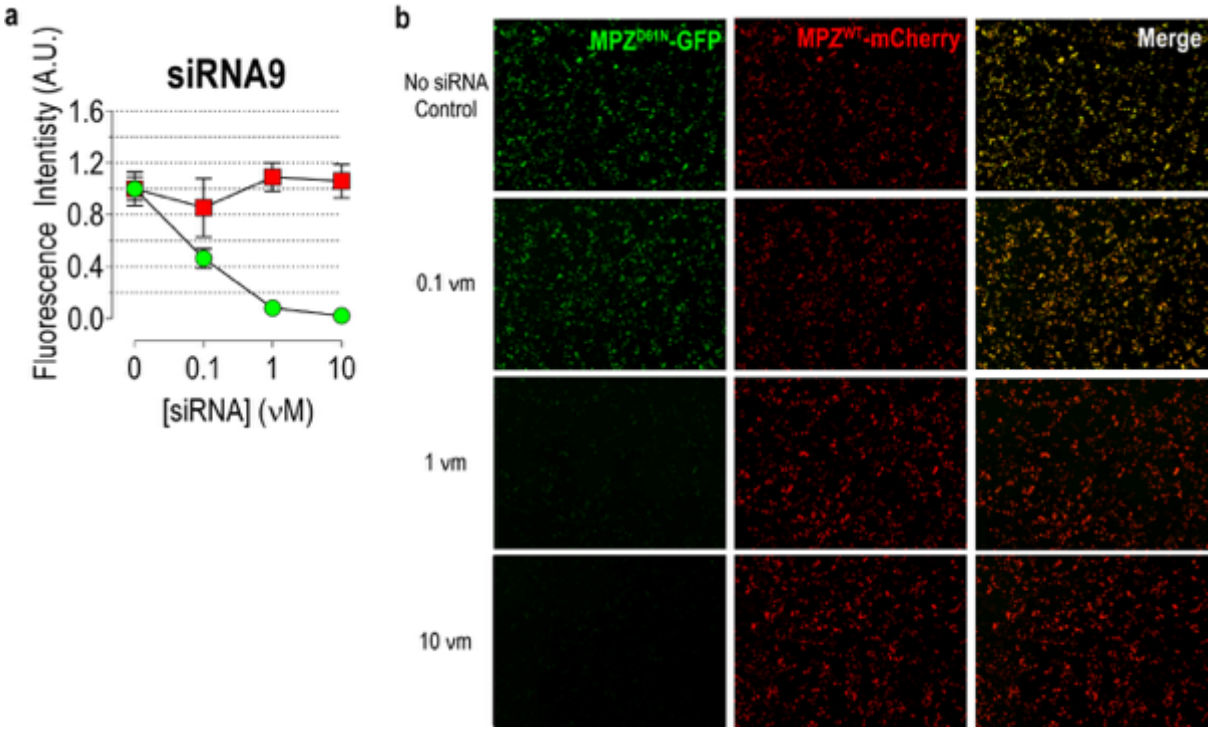

Supplementary Figure 6. Screening results for one of the siRNA sequences tested (siRNA9), showed as an example. (**a**) Fluorescence intensity quantification and (**b**) representative fluorescence images for one of the siRNA sequences showing high silencing efficacy and specificity.

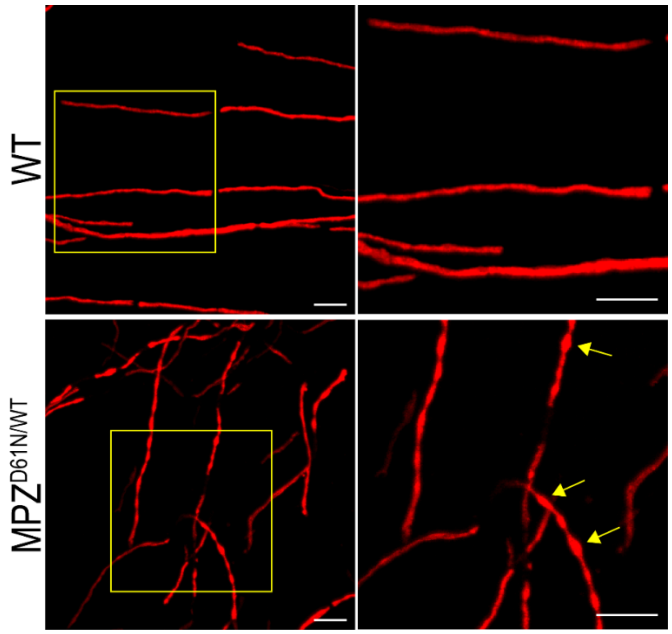

Supplementary Figure 7. Myelination defects of *Mpz*$^{D61N/WT}$ DRG cultures. Representative immunofluorescent stainings of WT and *Mpz*$^{D61N/WT}$ DRG cultures after three weeks in vitro. Cultures were immunostained for MBP (red). Images on the right are zoomed images of the regions highlighted by the yellow rectangles on the left. Yellow arrows indicate myelin abnormalities (that we called "focal hypermyelination sites") observed in mutant cultures. Scale bar: 20 µm.